

Article

Performance Evaluation of Radio Frequency Interference Measurements from Microwave Links in Dense Urban Cities

Michael Adedosu Adelabu ¹, Agbotiname Lucky Imoize ^{1,2,*}  and Glory Uzuazobona Ughegbe ¹ 

¹ Department of Electrical and Electronics Engineering, Faculty of Engineering, University of Lagos, Lagos 100213, Nigeria; madelabu@unilag.edu.ng (M.A.A.); gloryughegbe@yahoo.com (G.U.U.)

² Department of Electrical Engineering and Information Technology, Institute of Digital Communication, Ruhr University, 44801 Bochum, Germany

* Correspondence: aimoize@unilag.edu.ng; Tel.: +234-70-6783-4077

Abstract: Radio frequency interference (RFI) constitutes a significant problem in achieving a good quality of service in radio links. Several techniques have been proposed to identify and mitigate RFI in wireless networks. However, most of these techniques are not generalized for all propagation environments due to varying geographical features from one environment to another. The need for extensive frequency scan measurements on the links to identify the available channels, evaluate the performances of the links, and detect RFI in the channels becomes imperative. This study presents a performance evaluation of frequency scan measurements from active microwave links comprising eighteen base stations. The measurements equipment included a spectrum analyzer and a 0.6 m antenna dish. The frequency scans were taken at 6 GHz, 7 GHz, and 8 GHz with full azimuth coverage of the horizontal and vertical polarization. Measured data were processed to determine the available frequencies and RFI in the channels. The histogram and probability density function of the frequency scans were computed. The cumulative distribution functions were determined, and the statistical error characteristics of the frequency scans for the estimated normal distribution and the estimated fitness curve were derived. The short-time Fourier transform of the noisy signal was obtained, and the signal without noise was recovered using the inverse short-time Fourier transform. Analysis of the scanned signals before and after the noise removal is demonstrated. The denoised signals compare favorably with related results in the preliminary literature. Overall, these frequency scans would be beneficial in evaluating RFI measurements and spectrum planning and hold great promise for designing robust RFI detection algorithms for future wireless systems.

Keywords: cumulative distribution function; frequency bands; frequency scanning; polarization; interference detection and mitigation; probability distribution function; radio frequency interference; signal denoising; spectrum analyzer; statistical error analysis



Citation: Adelabu, M.A.; Imoize, A.L.; Ughegbe, G.U. Performance Evaluation of Radio Frequency Interference Measurements from Microwave Links in Dense Urban Cities. *Telecom* **2021**, *2*, 328–368. <https://doi.org/10.3390/telecom2040021>

Academic Editors: Peppino Fazio, Floriano De Rango and Carlos Tavares Calafate

Received: 24 July 2021

Accepted: 18 October 2021

Published: 19 October 2021

Publisher's Note: MDPI stays neutral with regard to jurisdictional claims in published maps and institutional affiliations.



Copyright: © 2021 by the authors. Licensee MDPI, Basel, Switzerland. This article is an open access article distributed under the terms and conditions of the Creative Commons Attribution (CC BY) license (<https://creativecommons.org/licenses/by/4.0/>).

1. Introduction

Radio frequency interference (RFI) poses a significant problem in offering good quality of service in wireless networks [1,2]. The interference could threaten the functionality of mobile network equipment due to the abnormal temperature occurring at the baseband processing units [3]. Several techniques have been proposed in the existing literature to mitigate RFI in wireless networks [4,5]. However, some conventional methods have not addressed the fundamental problem. Most traditional techniques remove a valuable portion of the desired signal alongside the unwanted signal [6]. Toward this end, several statistical, analytical, and experiment-based methodologies have been proposed to resolve the vast RFI issues in microwave radio links [4,7–9]. In particular, spectrogram analysis has been used to develop suitable RFI detection and mitigation algorithms in [4], factor analysis technique in [7], RFI experimentation in [8], and the narrow beam antenna pointing technique in [9]. However, these algorithms are not generalized to meet the requirements

of dynamic wireless propagation environments due to differences in the geographical terrains.

In recent times, reconfigurable intelligent surfaces (RIS) have been implemented to tackle this problem [10,11]. RIS is currently being designed to enable the envisioned 6G wireless networks just as massive MIMO is being utilized in the ubiquitous 5G wireless networks [12,13]. However, real-time control of the reflection amplitude and phase shift of RIS is achievable at a high design cost [14]. Moreover, the computational complexity of RIS-enabled signal processing systems remains an issue that needs to be resolved. Additionally, the available literature on RIS only presents the theoretical and simulation analysis of the system. There has been no detailed study on the practical deployment of RIS as an enabling technology to address the vast RFI issues in microwave radio links to the best of the authors' knowledge. Thus, the need to conduct comprehensive frequency scan measurements on active microwave links to evaluate the performances of the links and to detect and mitigate RFI in the channels is worthy of investigation. To this end, elaborate frequency scan measurements were conducted on three active microwave links at 6 GHz, 7 GHz, and 8 GHz by considering the horizontal and vertical polarization. The links comprised eighteen base transceiver stations. Several network parameters were measured with a spectrum analyzer and a 0.6 m antenna dish, covering the full azimuth with the vertical and horizontal polarization. The experimental data were processed and analyzed in MATLAB. The results are presented and discussed in Section 4 of this paper.

The primary focus of this paper is to evaluate the performance of microwave links using the radio frequency interference measurements obtained from the active links located in dense urban cities. These frequency scan measurements would provide reliable information for the detection and mitigation of RFI in the microwave links that were tested. The measured data will provide information on the best microwave link deployment techniques for optimum performance in dense urban environments. The data would provide insight on how to address microwave link design flaws resulting in RFI. The RFI data would provide valuable information on efficient frequency spectrum planning, analysis, assignment, and management. The dataset would help handle the concentration of the base transceiver stations transmitting at different frequencies in a spectrum, which poses a significant cause of RFI. Finally, the data would further support research and development towards the design and development of intelligent interference-resistant transceivers. The main contributions of the paper are summarized as follows:

1. Extensive field measurements to experimentally detect radio frequency interference in microwave links operating at the 6 GHz, 7 GHz, 8 GHz bands using a special-purpose spectrum analyzer;
2. We analyzed the actual frequency scan measurements for the horizontal and vertical polarizations at the operating frequency bands;
3. We conducted elaborate signal processing and analysis of the frequency scan measurements for the investigated links in the horizontal and vertical polarizations at the operating frequency bands;
4. Determination of the probability density functions of the frequency scans covering the normalized histogram, estimated normal distribution, normalized center lines, and the smoothed center lines;
5. Determination of the cumulative distribution functions of the frequency scans at the 6 GHz, 7 GHz, and 8 GHz bands for horizontal and vertical polarization;
6. Derivation of the statistical error characteristics of the frequency scans, including the mean absolute error (MAE), root mean squared error (RMSE), mean absolute percentage error (MAPE), relative absolute error (RAE), and mean squared error (MSE), each for the estimated normal distribution and the estimated fitness curve;
7. We conducted the denoising of the frequency scan signals and performed a comparative analysis of the scanned signals before and after the noise removal algorithm was applied.

The remaining parts of this paper are organized as follows. Section 2 presents the related literature and covers the existing RFI detection and mitigation algorithms and the emerging reconfigurable intelligent surfaces (RIS). Section 3 reports the materials and methodology—measurement campaign and signal processing of the frequency scan measurements. Section 4 presents the analyzed results and valuable discussions. Finally, the conclusion to the paper and future perspectives are given in Section 5.

2. Related Works

In the existing literature, several reports have been presented on radio frequency interference detection and mitigation [1,4,15]. RFI detection and mitigation techniques have been proposed previously [5,7,8]. Specifically, RFI detection and mitigation using compressive statistical sensing was proposed in [5]. Here, RFI detection and mitigation based on compressive statistical sensing of sub-Nyquist data is reported. The work aims at developing a real-time RFI detection and mitigation technique, adopting the cyclic spectrum analysis combined with compressive statistical sensing. However, the performance of the algorithm could not support hardware-based implementation. Factor Analysis (FA)-based RFI detection techniques were also proposed for satellite observations [7]. Additionally, RFI in satellite and terrestrial radio-relay systems is the subject of the investigation in [8]. Here, RFI measurements were conducted at 5.925 GHz and 6.425 GHz. The common signal interference in satellites and microwave radio relay systems was evaluated. However, additional data analysis would be required to determine the relative accuracy of RFI power flux density predictions.

RFI detection mechanisms for communication links were tested for terrestrial and geostationary satellite systems in [9]. Here, the radiated noise sources from an antenna bearing on a spacecraft at different amplitudes and frequencies were examined. The noise samples that were measured were compared with statistically calibrated data. Radio channels and multipath spatial consistency at frequencies below and above 6 GHz were reported [16]. The power angular spectrum (PAS), path angular profile (PAP), and angular distribution of paths were compared.

Furthermore, soil moisture active and passive (SMAP) radiometer observations of bandwidth, duration, and center frequency of RFI signals are presented in [17]. The work aimed to examine the properties and characteristics of RFI environments to determine the performance of RFI detection and mitigation algorithms. However, L-band RFI characteristics require rigorous analysis. In [18], the possibility of transporting a higher bandwidth via a single-mode fiber over a long distance is investigated. The results revealed that the losses on the transmitter are rather alarming due to RFI, though an amplified signal output of 22 dBm with an average noise figure of 1.4 dB was recorded.

RFI measurement survey was conducted in [19]. The work considers the 20 MHz to 6 GHz bands, uses a directional antenna, RF cable, and a spectrum analyzer. The authors aimed to detect strong intermittent and weak RFI signals on a radio telescope. An equation for the spectral flux density (SFD) was derived, and the SFD plots were analyzed to determine the presence of RFI in the main beam of the radio telescope. The study concluded that sites located around airport environments are practically not suitable for selection. In [20], a double-sideband modulation scheme was used to generate and transmit a dual-chirp microwave waveform to eliminate chromatic dispersion-induced power fading (CDIP) over fiber transmission. Different methods were employed to create dual-chirped microwave waveforms. Worthy of mention is the deficiency suffered by the dual-chirp microwave waveform from the periodic attenuation of the signal power. An anti-dispersion transmission scheme was deployed to counter this deficiency. A one-to-multi-anti-dispersion transmission link of the dual-chirp microwave signal was evolved, leading to an appreciable elimination of the CDIP using the proposed scheme.

The Z-shape spoof-surface plasmon polaritons structure was employed towards a dual-frequency-scanning broadband antenna at 2.8–7.3 GHz and 13.7–27.4 GHz [21]. The geometric parameters of the Z-shape unit cell were adjusted. The work was tested by

fabricating a prototype dual-frequency-scanning broadband antenna on the F4B substrate using PCB. The proposed frequency scanning on the two frequency bands was achieved concurrently. However, this is not readily applicable to the higher frequency bands.

Furthermore, Maxwell's equations and the reciprocity theorem have been used to determine the transfer function of the observed RFI in radio links [22]. Additionally, a decision tree model incorporating a machine learning algorithm has been deployed to suppress RFI in nuclear quadrupole resonance (NQR) data [23]. However, this methodology may not apply to low-level or continuous background RFI scenarios.

Reconfigurable intelligent surfaces (RIS) are currently gaining widespread popularity as enabling technologies to tackle the vast RFI issues in wireless networks. RIS is envisioned to enable 6G wireless networks similarly to the use of massive MIMO in 5G wireless networks [12,13]. In the recent literature [24,25], RISs have been identified as candidate technologies to improve the performance of wireless communication networks with minimal or no interference. Interestingly, RIS is relatively passive, requiring fewer active antennas at the BS to achieve massive MIMO gains [26]. This lends credence to the high energy efficiency of RIS [27]. Generally, RISs, owing to the passive elements used in their design, can mitigate the impact of interference in an ultra-dense wireless network [28].

Comparatively, an RIS has a meager cost relative to other relay-based technologies. RIS is sometimes referred to as large intelligent surfaces [29,30]. Moreover, RIS facilitates low-power device-to-device (D2D) communication, leading to the actualization of simultaneous wireless information and power transfer (SWIPT) [28,31]. They are often referred to as reconfigurable intelligent surfaces [27,32] and software-controlled metasurfaces [33]. Currently metasurfaces are being designed with the conventional reflect arrays [34,35], liquid crystal arrays [36], or software-defined metamaterials [33,37]. Due to their passive nature, RISs can easily be deployed on buildings and other structures. RISs can be configured to achieve security at the physical layer [28,38]. A typical RIS-assisted wireless communication system that reflects signals from the RIS to facilitate seamless communication between the BS, and the mobile station is given in Figure 1 [39]. An analysis of RIS features compared to existing relay systems is presented in Table 1 [39].

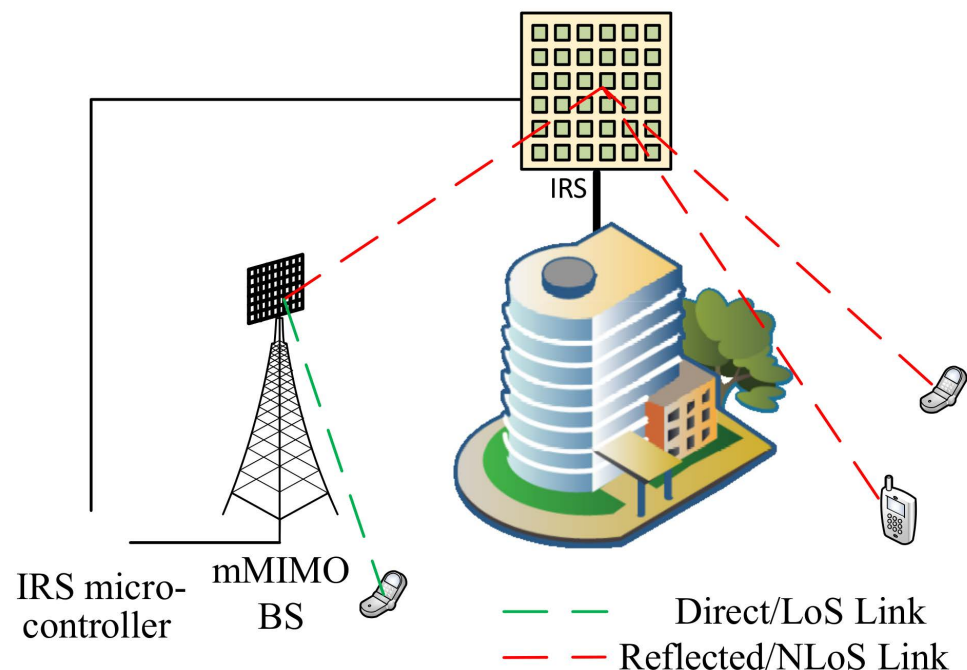


Figure 1. Illustration of a Reconfigurable Intelligent Surface (RIS)-assisted communication system.

Table 1. A comparative analysis of RIS features with other relay systems.

Features	Reconfigurable Intelligent Surfaces (RIS)	Active, Intelligent Surface-Based Massive MIMO	Backscatter Communication	Amplify and Forward Relay
Hardware architecture	Passive elements	Active elements	Active elements	Active elements
Power consumption	Low	High	High	High
Environment propagation control	Adjusts the phase shift through intelligent controllers.	-	Reflects received signals from external sources like TV.	-
Noise effect	Only reflects the received signal	The use of artificial noise is helpful to the system [40].	The backscatter signals are weak and with a low signal-to-noise ratio.	Amplifies received signal and receiver noise
The unit cost of deployment	Low	High	Low	Low

Despite the auspicious potentials of RIS in facilitating beyond 5G wireless communication systems, several challenges have been identified [41,42]. Specifically, the phase range of unit cells making up the aperture is relatively limited [41]. This implies that a complex cell topology would be required to achieve a full-phase range. Consequently, this tends to increase the hardware complexity [42]. Additionally, real-time control of the reflection amplitude and phase shift of RIS could be computationally expensive [14]. Currently, RIS lacks radio resources for perfect channel estimation [43]. This makes it quite challenging to estimate channel state information [25,44]. A low-power RF chain-empowered RIS capable of channel estimation has been proposed [28] to alleviate this limitation. Interestingly, a ray-tracing technique [45] was recently presented to estimate the channel information by [32], and machine learning, deep learning, and federated learning models have been provided to tackle these challenges at reduced costs [46–48]. However, the lack of adequate test and training data has limited the use of machine learning-based RIS schemes. The related literature, including the key contributions, findings, and limitations, are summarized in Table 2.

Table 2. Summary of related works, including contributions, key findings and limitations.

Refs.	Scope and Focus	Contributions	Limitations
[1]	Radio frequency interference measurements. Several measurements and testing equipment were deployed.	Sporadic, continual, and equipment-related signals causing interference were identified during the extensive RFI measurements.	Though grounding systems were installed to mitigate the impact of sporadic emissions, those linked to wind blowing remain.
[4]	Radio frequency interference detection and mitigation algorithms.	Several RFI detection and mitigation algorithms by two-dimensional filtering were derived, leveraging spectrogram analysis.	The algorithms were only tested with sinusoidal, chirp, PRN, and OFDM-like signals. The need to test other types of RFI signals with these algorithms remains.
[5]	Radio frequency interference detection and mitigation	Compressive statistical sensing (CSS) was introduced to detect and mitigate radio frequency interference.	Further analysis to determine the actual performance of the algorithm under a hardware-based implementation is required.
[7]	Radio frequency interference detection on satellite observations.	A factor analysis-based method was proposed for radio frequency interference detection on satellite observations.	RFI detection uncertainties associated with the proposed method remain due to the lack of independent validation datasets.
[8]	Radio frequency interference measurement experimentation	A new proposition on using a geostationary satellite with a high gain, steerable antenna to survey the Earth for sources of potential RFI was reported.	Further data analysis is required to determine the relative accuracy of predictions for RFI power flux density.
[9]	Systems and methods for determining radio frequency interference	A new technique involves pointing a narrow beam antenna on the satellite at the terrestrial region to determine the presence, frequency, and amplitude of radio frequency interference superimposed on communication.	The systems and methods described appear quite complex and may pose huge design costs.

Table 2. Cont.

Refs.	Scope and Focus	Contributions	Limitations
[15]	A review of RFI mitigation techniques in microwave radiometry, including real aperture and aperture synthesis techniques, was covered.	Discussion and assessment of the application of RFI mitigation techniques were presented. The feasibility of RFI detection and mitigation at one bit and level two is restated.	The findings from the survey would require further experimentation for results validation.
[17]	L-Band radio frequency interference environment	Characterization of the L-Band radio frequency interference environment using SMAP radiometer observations	Further analysis of the L-band RFI characteristics based on their temporal and spatial distributions is required.
[19]	Radio frequency interference site survey for radio telescopes in Thailand.	The variability of the signal intensity according to the presence of the neighboring population and topography is investigated.	More intensive RFI measurements at some of the sites are required to validate the results.
[22]	Transfer function-based calculation method for radio frequency interference.	A transfer function-based calculation method is proposed to estimate RFI problems. Closed-form equations are analytically derived from Maxwell's equations and the reciprocity theorem.	Though numeric simulations and real cellphone experiments have been reported, further insights are required to ease the practical implementation of the equations.
[23]	Radio frequency interference suppression in NQR experiments	A decision tree pattern recognition model was developed for radio frequency interference suppression in NQR experiments.	Sensitivity is not assessed because the ROC curves do not discriminate the data as a function of the sample mass.
[24]	Power control for physical-layer broadcasting using intelligent reflecting surface aided network	A joint design of the transmit beamforming at the BS and the phase shifts of the RIS units. Derivation of the lower bound of the minimum transmits power for the broadcast setting.	Only analytical and simulation results are reported. Experimental implementation remains.
[25]	Intelligent Reflecting Surface-Enhanced Wireless Network via Joint Active and Passive Beamforming	Joint optimization of the (active) transmit beamforming at the AP and (passive) reflect beamforming by the phase shifters at the IRS to minimize the total transmit power at the AP under a given set of signal-to-interference-plus-noise ratio (SINR) constraints at the user receivers	Effective self-interference cancellation (SIC), which incurs more energy consumption, would be required to achieve spectrum efficiency
[28]	Smart and reconfigurable environment: intelligent reflecting surface aided wireless network	An overview of the promising RIS technology for achieving a smart and reconfigurable environment in future wireless networks.	Practical deployment of the RIS is not covered in work.
[30]	Passive beamforming and information transfer via large, intelligent surface	A PBIT-enhanced wireless system, in which a LIS simultaneously enhances the user-BS communication and transmits information to the receiver, is proposed.	The numerical results show that the proposed PBIT system is superior to the preliminaries. However, practical implementation of the LIS-enabled system remains.
[43]	Intelligent reflecting surface assisted wireless communication: modeling and channel estimation	A minimum means squared error-based channel estimation protocol for the design and analysis of IRS-assisted systems was proposed.	Experimentally validated channel models that provide pathloss and fast fading parameters for IRS-assisted links under different implementations are required.

From the preceding, it is apparent that most of these algorithms are grossly limited in design and performance. That being said, some of these algorithms perform well when deployed in the environments for which they have been designed. However, their accuracy is questionable when deployed in other geographical settings. Additionally, most of the existing RFI detection and mitigation schemes require experimental validation. To this end, the need to conduct extensive frequency scan measurements geared towards evaluating the performance of the radio links and developing more generalized RFI detection and mitigation algorithms is vitally important. Thus, we present extensive frequency scan measurements obtained using a special purpose spectrum analyzer. The measurement campaign was conducted on active microwave links comprising eighteen base stations located in selected dense urban cities in Nigeria. The materials used and the methodology of obtaining the frequency scan measurements are briefed in Section 3 of this paper.

3. Materials and Methods

The measurement campaign and the investigate environments are presented in Section 3.1. The methodologies used for result processing and analysis are given in

Section 3.2. Here, helpful information about the measurement environments, the equipment used, and experimentation procedures are broached. Additionally, the method for result processing and analysis is highlighted in this section.

3.1. Measurement Campaign

The experimental frequency scan measurements were conducted in two densely populated urban cities in the Kogi and Lagos States in Nigeria. The densely populated cities are located in different geo-political zones, in the south-west and north-central regions, respectively [49,50]. These areas have been chosen due to the location of the microwave links and ease of access. Additionally, such environments have recently been described as fast-growing urban cities [51]. The need to test the performance of the microwave links in such cities to know the impact of RFI on the links has become imperative. A graphical representation of the geographical coordinates of the measurement environments is given in Figure 2.

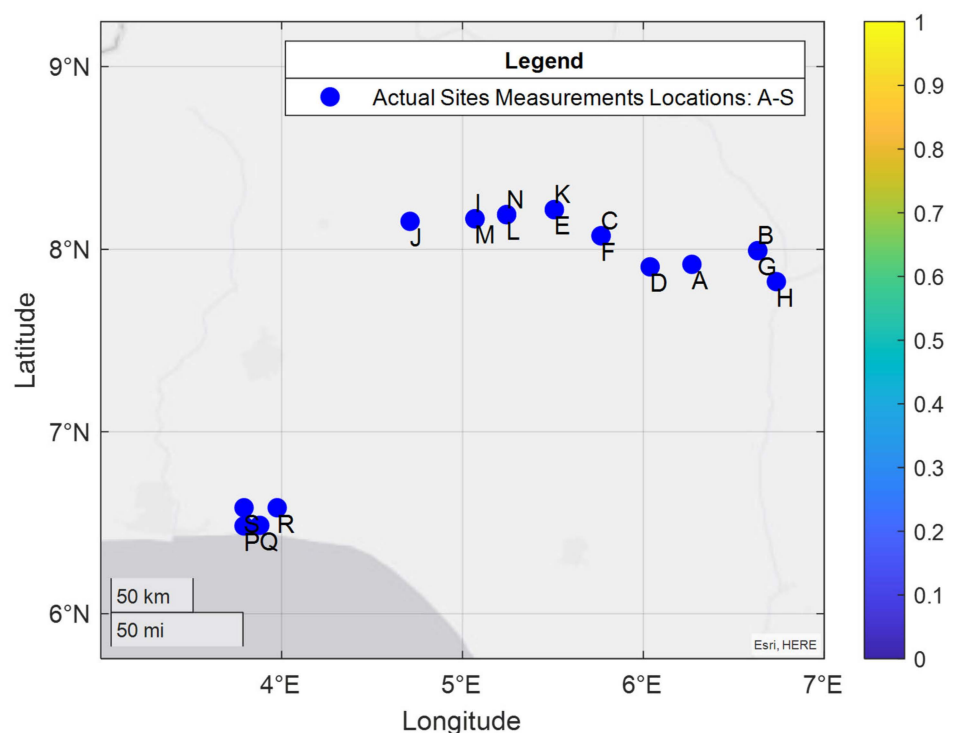


Figure 2. The geographical coordinates of the measurement environments.

The measurements equipment deployed to the microwave link locations in these cities comprised a spectrum analyzer-Anritsu model MS2724C [52] and a 0.6 m antenna dish [3]. The spectrum analyzer ranged from 9 kHz to 20 GHz. The broadband preamplifiers over the whole frequency range for increased sensitivity was approximately 17 dB. A hardware description of the experimental setup for the frequency scan measurements is as shown in Figure 3. Here, the fixed base transceiver station, the spectrum analyzer, and the 0.6 m antenna are depicted. The frequency bands that were tested included the 6 GHz, 7 GHz, and 8 GHz bands. The frequency usage plan for the various frequency bands that were investigated is given in Table 3. The measurements covered the full azimuth and the vertical and horizontal polarizations for all scenarios. The spectrum master was chosen due to its design capabilities, making it suitable for RF testing and microwave link troubleshooting. Additionally, the analyzer can detect spurious signals and radio frequency interference in the microwave radio links. Furthermore, it is very flexible and relatively easy to operate with minimal difficulty.

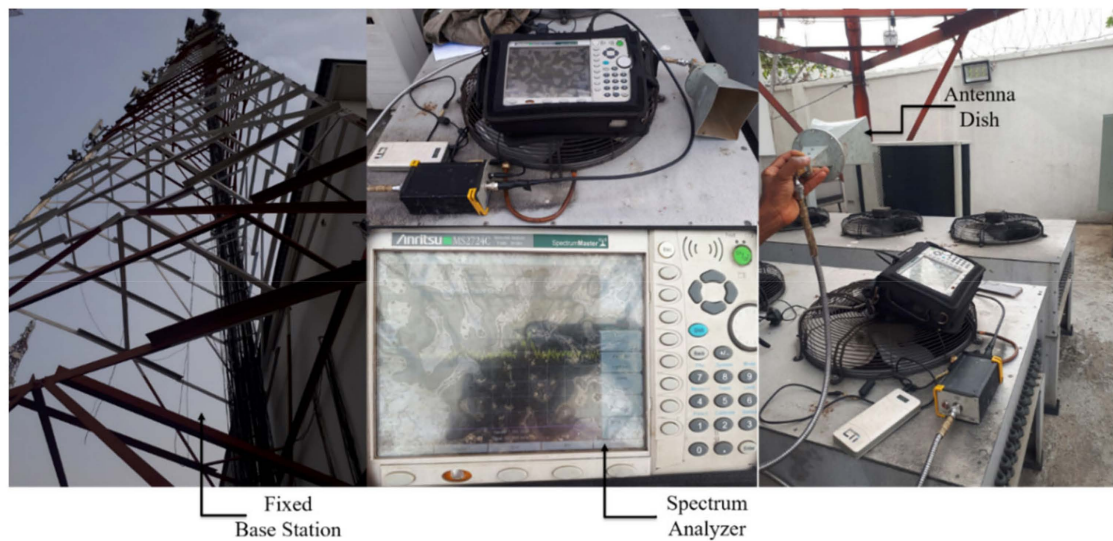


Figure 3. Experimental setup for the frequency scan measurements.

Table 3. Frequency usage plan for the three different frequency bands tested.

Frequency Band	Start Frequency	Stop Frequency	Frequency Span
6 GHz	5.9 GHz	6.5 GHz	600 MHz
7 GHz	7.4 GHz	7.8 GHz	400 MHz
8 GHz	7.7 GHz	8.3 GHz	600 MHz

In order to start the frequency scan measurements, we made two selections to set the frequency range of the analyzer. The frequency knobs were adjusted appropriately to start and stop, and these settings were utilized for the sweeping exercise. In addition, we scanned the desired frequency span from the lowest to the highest frequency band in the tested frequency range. Additionally, we set the speed of the scan on the spectrum master to scan the frequency range for a faster measurement completion time. Furthermore, we adjusted the scanning mode feature on the analyzer to display the signal strength or amplitude. This feature was used to monitor the amplitude variations and frequency in the uplink on the analyzer. The output gives valuable information on the most suitable frequency and severe interference in the scanned frequencies. The in-phase and quadrature (I/Q) data were also derived using the time/amplitude and frequency details obtained from the baseband processing by sliding a spectrum window across the tested frequency spectrum as an amplitude function. Additionally, the analyzer was connected to the fixed antenna and was allowed to sweep for a day. In this case, the scan measurements were saved to the analyzer at an hour interval, and the scans were then extracted to a personal computer for further processing. Finally, the frequency scan measurements were analyzed in MATLAB, and the results are presented in Section 4 of this paper.

3.2. Measured Signal Processing

The measured signals were recreated in the MATLAB environment to investigate their characteristics. The first step was determining the sampling rate. It is assumed that the offset frequency is the start frequency for each band. Since the spectrums are plotted as a one-sided spectrum, the sampling rate (f_s) of the input signal is as given in Equation (1).

$$f_s = 2F_s \quad (1)$$

where F_s is the frequency span.

Thus, the sampling frequencies are obtained as 1.2 GHz, 0.8 GHz, and 1.2 GHz for the 6 GHz, 7 GHz, and 8 GHz frequency bands.

The signals are generated as sine waves and colored noise. Figure 4 shows the process of generating colored noise. The signals are fed as inputs to the random stream generator. The output of the random stream generator is white noise, which could be Gaussian or uniform. This is fed to the coloring filter, and the colored noise is evolved after applying the appropriate gain factor.

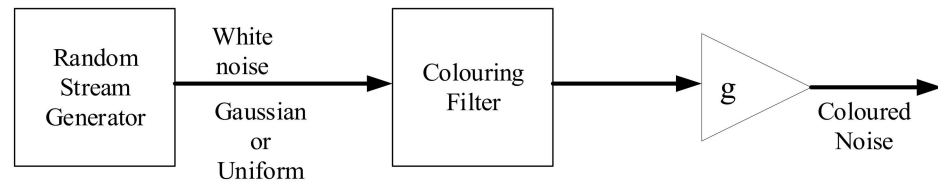


Figure 4. Process of generating colored noise.

The random stream generator generates a white noise that is either a Gaussian or uniform distribution. Uniform white noise has its amplitude bounded between +1 and −1, while Gaussian noise amplitude is not bounded between +1 and −1. This boundary is enforced by the gain g . A coloring filter is then applied to the generated white noise, with a power spectral density (PSD) given in Equation (2).

$$S(f) = \frac{L(f)}{|f|^\alpha} \quad (2)$$

where α is the inverse frequency power in the interval $-2 \leq \alpha \leq 2$. α is a real number. $L(f)$ is a positive, slowly varying, or constant function. If $\alpha = 0$, then no coloring filter is applied to the generated white noise, and $L(f)$ is a constant proportional to the process variance. If $\alpha > 0$, $S(f)$ goes to infinity as the frequency, f , approaches 0. If $\alpha < 0$, the process is anti-persistent and exhibits a negative correlation between increments.

The sine waves were generated with the trigonometric function method, which computes the sinusoid in the i th channel, y_i by sampling the continuous function as expressed in Equation (3).

$$y_i = A_i \sin(2\pi f_i t + \varphi_i) \quad (3)$$

where A_i is the amplitude of the i th channel, f_i is the i th channel frequency, and φ_i is the phase offset. Each band and polarization for all of the scans can then be generated by adding all of the signals at different frequencies, as given in Equation (4).

$$S_{b,p} = \sum_i^N y_i \quad (4)$$

Equation (5) expresses the power of the signal concerning its standard deviation (σ) [53]. Therefore, the standard deviation (σ) can be described, as shown in Equation (6). It is assumed that the default Gaussian noise in the environment has the standard deviation as calculated in Equation (6) with zero mean. Otherwise, if a particular frequency is used, a signal is generated and added to the Gaussian noise. The step-by-step procedure for the analysis of the scanned frequencies is given in Table 4.

$$p = 10 \log_{10} \sigma^2 \quad (5)$$

$$\sigma = \sqrt{10 \frac{p}{10}} \quad (6)$$

Table 4. Step-by-step procedure for measured data processing and analysis.

S/N.	Procedure	Specific Task
1.	Replicating the spectrum analyzer frequency scans	<ul style="list-style-type: none"> (a) Specify the sample rate frequency; (b) Specify the offset frequency; (c) Specify the number of averages; (d) Determine the type of noise at the site; (e) Specify the power of the noise; (f) Generate signals at specified frequencies, as shown in the scans.; (g) For multiple scan results on a graph, specify the number of input ports.
2.	Statistical characteristics	<ul style="list-style-type: none"> (a) Generate the histogram of the site scan data; (b) Observe the distribution of the generated histogram and then generate an approximate distribution for the data; (c) For the site data, obtain the mean, median, standard deviation, variance, interquartile range, skewness, and Kurtosis; (d) For the estimated distribution, obtain the negative loglikelihood, lower and upper confidence intervals for the standard deviation; (e) Generate a line graph connecting the centers of the histograms; (f) Generate a smooth line approximating the generated line graph using 9th order polynomial.
3.	Error Analysis for each of the approximated distributions and generated smoothed line	<ul style="list-style-type: none"> (a) Obtain the following statistical parameters between the actual site data and each of the estimated distribution and generated smoothed lines: Mean Absolute Error (MAE); Root Mean Square Error (RMSE); Mean Absolute Percentage Error (MAPE); Mean Squared Error (MSE); Relative Absolute Error (RAE). (b) Generate the probability distribution function and the cumulative distribution functions.
4.	Signal denoising process	<p>The step-by-step process of the signal denoising is described as follows:</p> <ul style="list-style-type: none"> (1) Using a suitable window, obtain the short-time Fourier transform (STFT) of the noisy signal; (2) Square the absolute values of the results obtained in (1); (3) Sort the results obtained in (2) in descending order; (4) Obtain the cumulative sum of the results obtained in (3); (5) Identify the values of (4) that have more than 30% of the power. Set this as the threshold value; (6) Find the values of (2) that are greater than the threshold value; (7) The next step is the denoising of the signal through multiplying (1) by (6); (8) Recover the signal without noise through inverse short-time Fourier transform (ISTFT).

3.3. RFI Mitigation Technique

The existing signals in the channels are treated as noise that needs to be suppressed to deploy other valuable signals in the same frequency band. The signals can be represented in the time–frequency domain. Short-time Fourier transform (STFT) and inverse short-time Fourier transform (ISTFT), a Fourier transform pair, have been used for the analysis. This agrees with the methods used by Hristo [54,55].

3.3.1. Short-Time Fourier Transform (STFT)

Let $s(n)$ be a real-world signal with N samples and $0 \leq n \leq N$. The STFT of each segment k is the discrete Fourier transform (DFT) of $s(n)$, as shown in Equation (7).

$$S(k) = \sum_{m=1}^N s(m)e^{-j2\pi\frac{mk}{N}} \quad (7)$$

The DFT is implemented by fast Fourier transform (FFT) is similar to that proposed by Frigo and Johnson [56–58]. The signal frames $s(m)$ at regular intervals can be expressed as shown in Equation (8).

$$s(m) = s_h(m)w(m) \quad (8)$$

$w(m)$ is the window function, $1 \leq m \leq M$. M is the analysis window length, $M \leq N$. To improve the performance of the FFT algorithm, the signal $s(m)$ is padded with zeros such that $2^{(2^N)} \geq M$. Here, $s_h(m)$ is the signal frame expressed concerning the hop size. Hop size is the time advance from frame m to $m + 1$. $s_h(m)$ is expressed as shown in Equation (9).

$$s_h(m) = s(m + lh) \quad (9)$$

l is the frame index, and $0 \leq l \leq L - 1$. L is the total number of frames: $L \leq N$.

Given a sampling frequency f_s , the linear frequency vector (f) can be expressed as shown in Equation (10).

$$f = \frac{nf_s}{N} \quad (10)$$

Similarly, the time vector (t) can be calculated using Equation (11).

$$t = \frac{lh}{f_s} \quad (11)$$

Therefore, given a signal $s(n)$ with a window function $w(m)$, a hop size h , with N total samples, and that was sampled at f_s frequency, the STFT $S(k)$, the frequency vector f , and the time vector t can be calculated by Equation (7), Equation (10), and Equation (11), respectively.

3.3.2. Inverse Short-Time Fourier Transform (ISTFT)

In order to reconstruct the original signal, the inverse short-time fast Fourier transform (ISTFT) [59] of the signal is evaluated. Similar to the STFT, the inverse discrete Fourier transform (IDFT) [60] is achieved by using the inverse fast Fourier transform (IFFT), as shown in Equation (12). The window function, as a weight for the reconstruction, as shown in Equation (13), where $v(m)$ is the window function; $w(m)v(m)$ is the overlap-add (OLA) function.

$$\tilde{s}(m) = \frac{1}{N} \sum_{k=1}^N S(k)e^{+j2\pi\frac{mk}{N}} \quad (12)$$

$$\tilde{s}(n) = \frac{h}{w(m)v(m)} \tilde{s}(m)v(m) \quad (13)$$

3.3.3. Window Function

Several window functions, such as Blackman, Blackman–Harris, Hann, Hamming, etc., have been reported [61]. However, the Hann and Hamming window functions perform better for the weighted overlap–add (WOLA) computations. Therefore, the Hann and Hamming window functions were used for the data analysis. The signal denoising process is also given in Table 4. The results of the denoised signals and helpful discussions are presented in Section 4 of this paper.

4. Results and Discussions

The extensive frequency scan measurements for the 18 channels at the 6 GHz, 7 GHz, and 8 GHz bands in horizontal and vertical polarization are presented in this section. The results reported here include the available and not available frequencies. The actual frequency scans analyzed in MATLAB include the probability density functions (PDF), cumulative distribution functions (CDF), and error statistics. In particular, Section 4.1 gives the results of the frequency scan measurements. Section 4.2 presents the histogram and probability density function of the frequency scan measurements, Section 4.3 presents the cumulative distribution functions, and Section 4.4 reports the statistical error analysis.

Furthermore, Section 4.5 gives the results of the measured signal denoising. Section 4.6 presents a comparison of the signal before and after denoising. Section 4.7 shows a brief comparison of the results with related works. Finally, Section 4.8 gives a concise discussion of the results.

4.1. Frequency Scan Measurements

This only section presents the results showing the availability of the desired frequencies for the eighteen channels tested at 6 GHz for brevity. First, we categorized the channels that were available and not available, as given in Table 5. The letter A means that the desired frequency was available, and NA means that the desired frequency was not available. Next, we show the results for the 18 channels scanned with the spectrum analyzer for the 6 GHz, 7 GHz, and 8 GHz bands in both polarizations. Specifically, Figure 5 shows the 18 channels scanned with the spectrum analyzer for the horizontal polarization of the 6 GHz band. Figure 6 gives the vertical polarization scan for the 6 GHz band for all 18 sites. Figure 7 shows the 7 GHz horizontal polarization scan for all 18 sites. Figure 8 presents the 7 GHz vertical polarization scan for all 18 sites, Figure 9 shows the 8 GHz horizontal polarization scan for all 18 sites, and Figure 10 gives the 8 GHz vertical polarization scan for all 18 sites.

Table 5. The desired frequencies for the 18 channels at 6 GHz: Available (A); Not Available (NA).

Freq.	A	B	C	D	E	F	G	H	I	J	K	L	M	N	P	Q	R	S
5.945	A	A	A	A	A	NA	NA	NA	A	NA	NA	A	A	A	A	A	A	A
5.975	A	A	A	A	A	NA	NA	NA	A	A	NA	A	NA	A	A	A	A	A
6.005	A	A	A	A	A	NA	NA	NA	A	NA	A	A	A	A	A	A	A	A
6.034	A	NA	A	NA	A	NA	NA	NA	A	NA	NA	A	A	A	NA	NA	A	A
6.093	A	A	A	NA	A	NA	NA	NA	A	A	NA	A	A	A	A	A	A	A
6.153	A	A	A	A	A	NA	NA	NA	A	A	A	A	A	A	NA	NA	A	NA

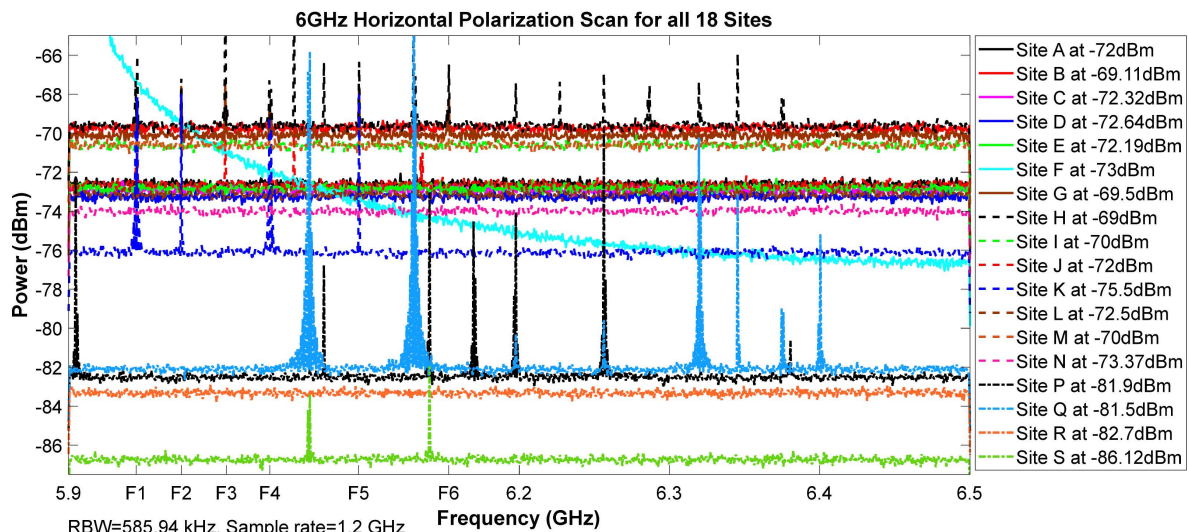


Figure 5. 6 GHz horizontal polarization scan for all 18 sites.

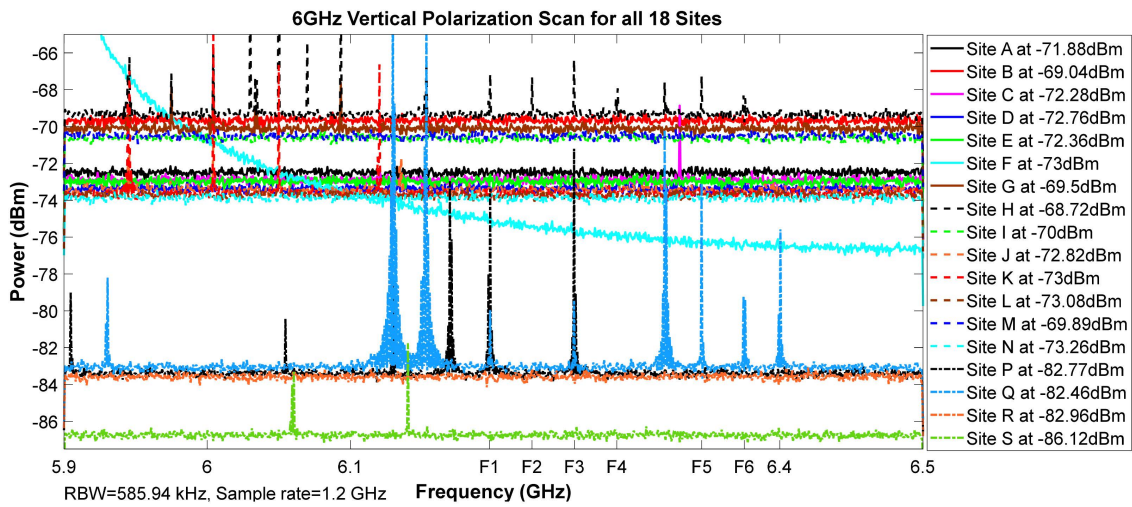


Figure 6. 6 GHz vertical polarization scan for all 18 sites.

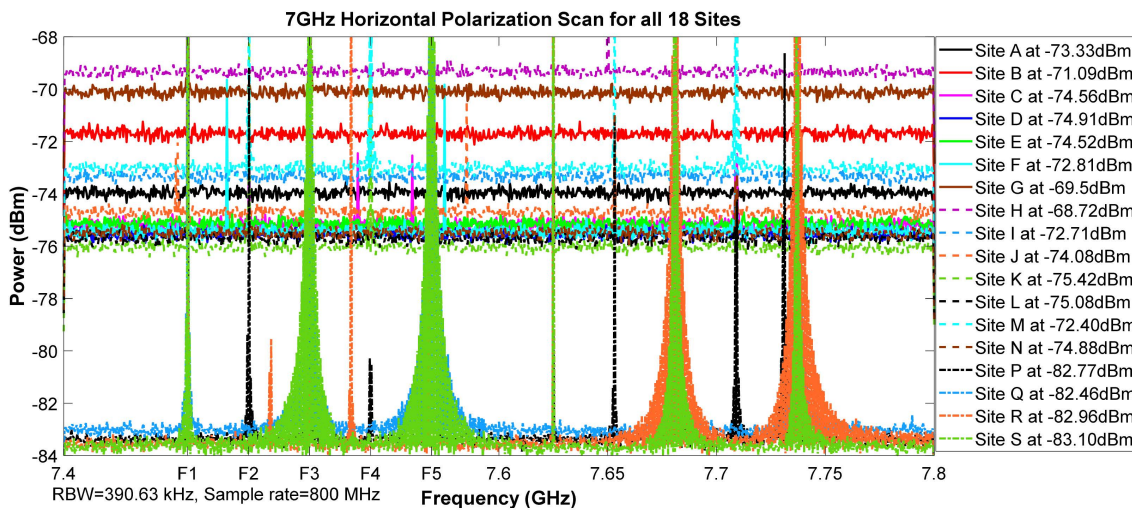


Figure 7. 7 GHz horizontal polarization scan for all 18 sites.

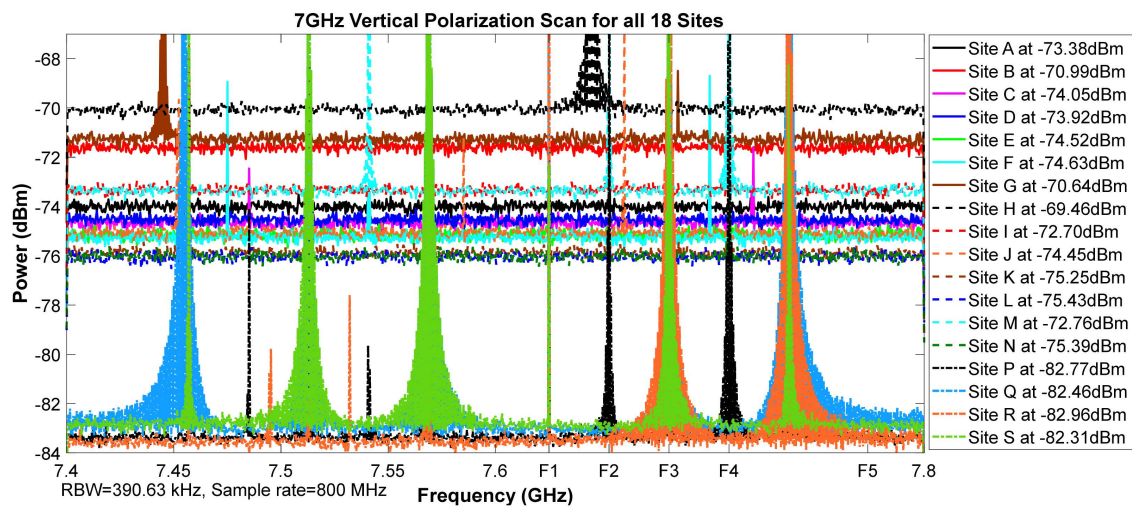


Figure 8. 7 GHz vertical polarization scan for all 18 sites.

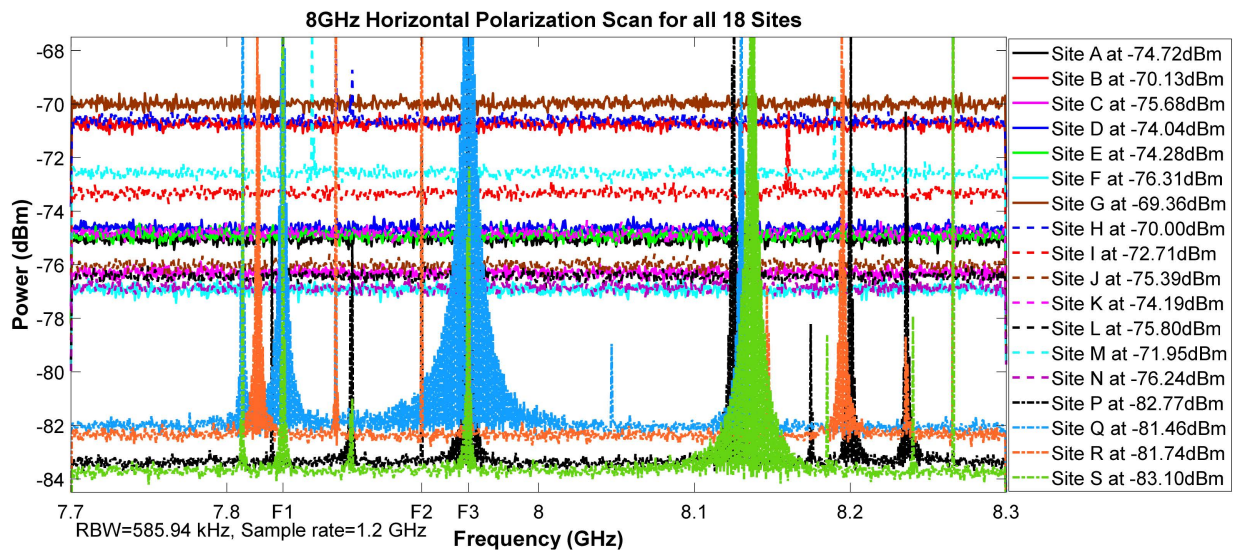


Figure 9. 8 GHz horizontal polarization scan for all 18 sites.

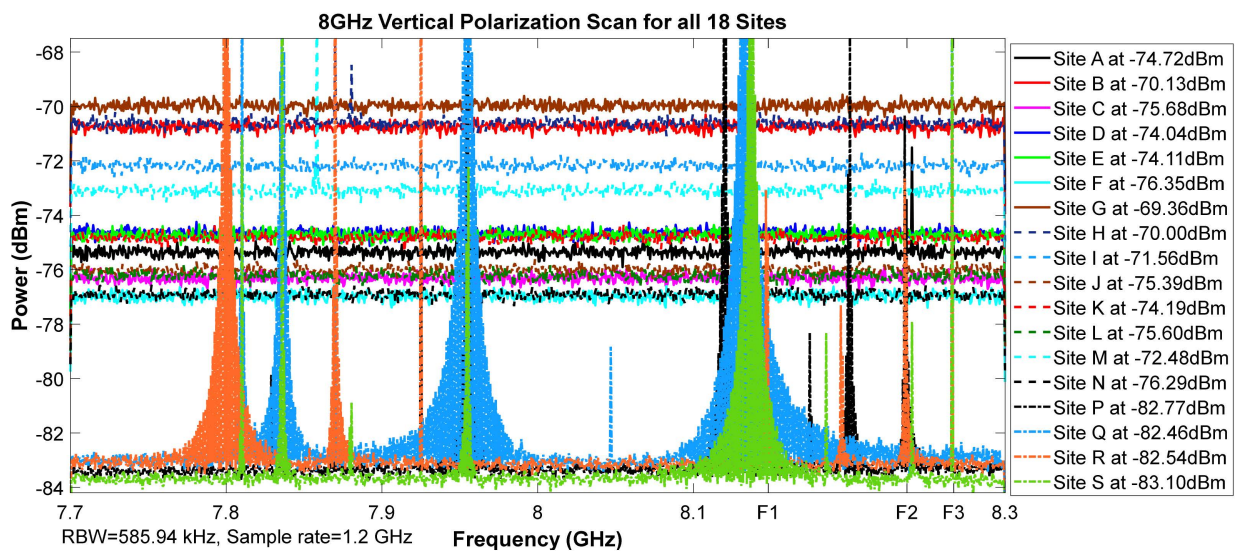


Figure 10. 8 GHz vertical polarization scan for all 18 sites.

4.2. Histogram and Probability Density Function

The histogram and probability density function (PDF) of the frequency scan measurements are presented. These comprise the normalized histogram, estimated normal distribution, normalized center lines, and the smoothed center lines. In particular, Figure 11 gives the histogram and PDF of the frequency scan for site A at the 6 GHz horizontal polarization. Figure 12 shows the histogram and PDF of the frequency scan for site B at the 6 GHz horizontal polarization. Figure 13 presents the histogram and PDF of the frequency scan for site C at the 6 GHz horizontal polarization. Figure 14 shows the histogram and PDF of the frequency scan for site D at the 6 GHz horizontal polarization. Figure 15 depicts the histogram and PDF of the frequency scan for site A at the 6 GHz vertical polarization. Figure 16 shows the histogram and PDF of the frequency scan for site B at the 6 GHz vertical polarization.

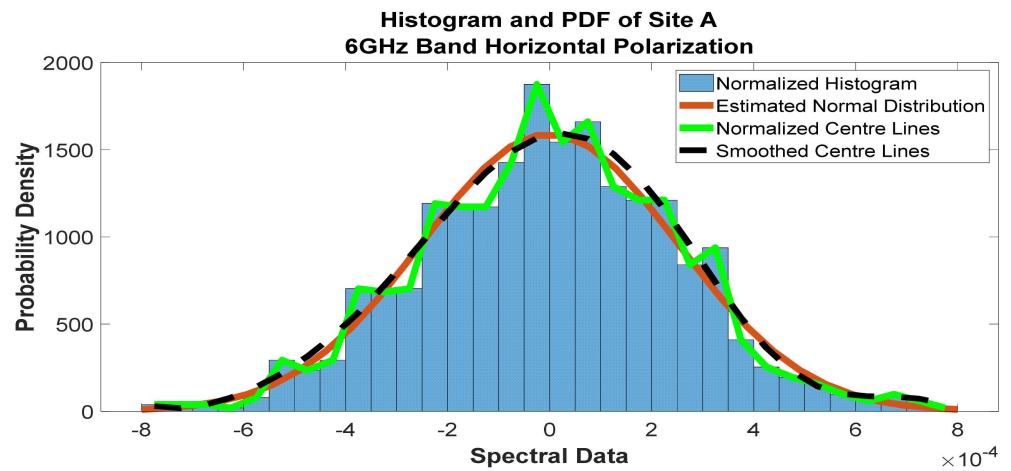


Figure 11. Histogram and PDF of the frequency scan for site A at 6 GHz horizontal polarization.

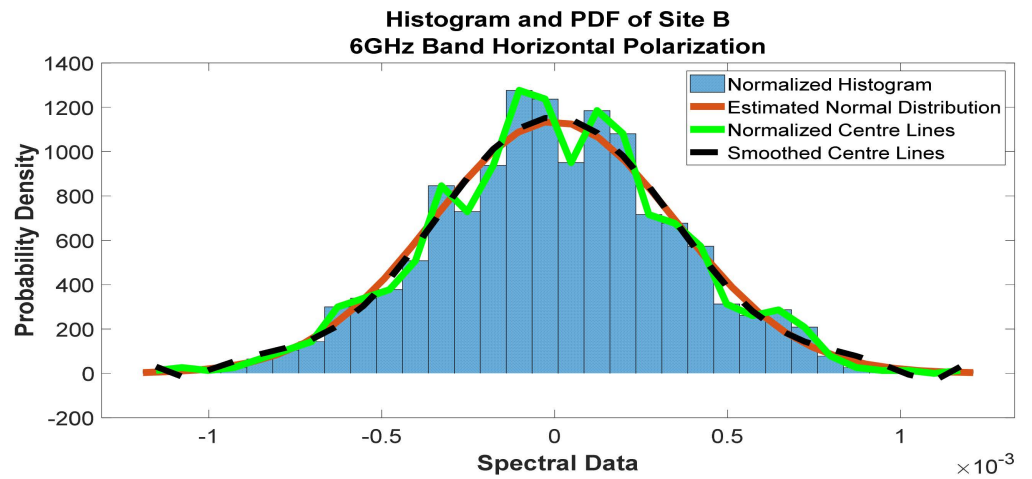


Figure 12. Histogram and PDF of the frequency scan for site B at 6 GHz horizontal polarization.

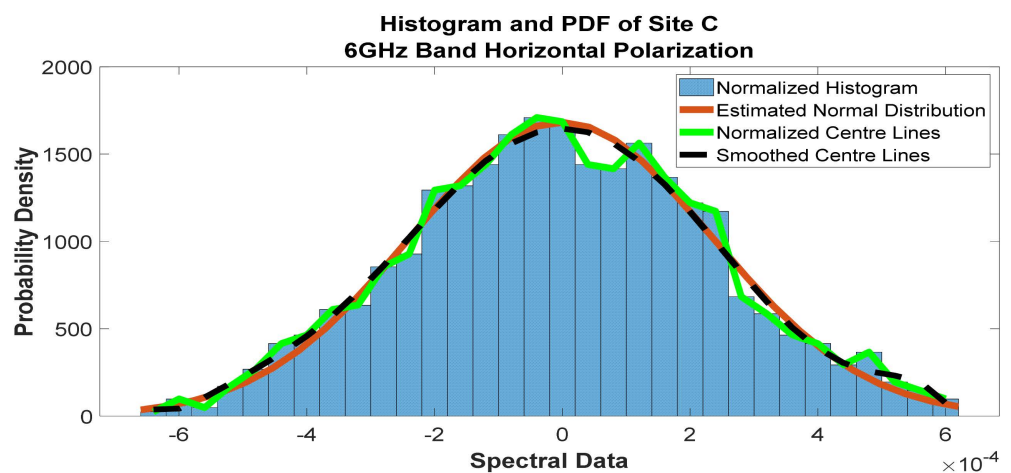


Figure 13. Histogram and PDF of the frequency scan for site C at 6 GHz horizontal polarization.

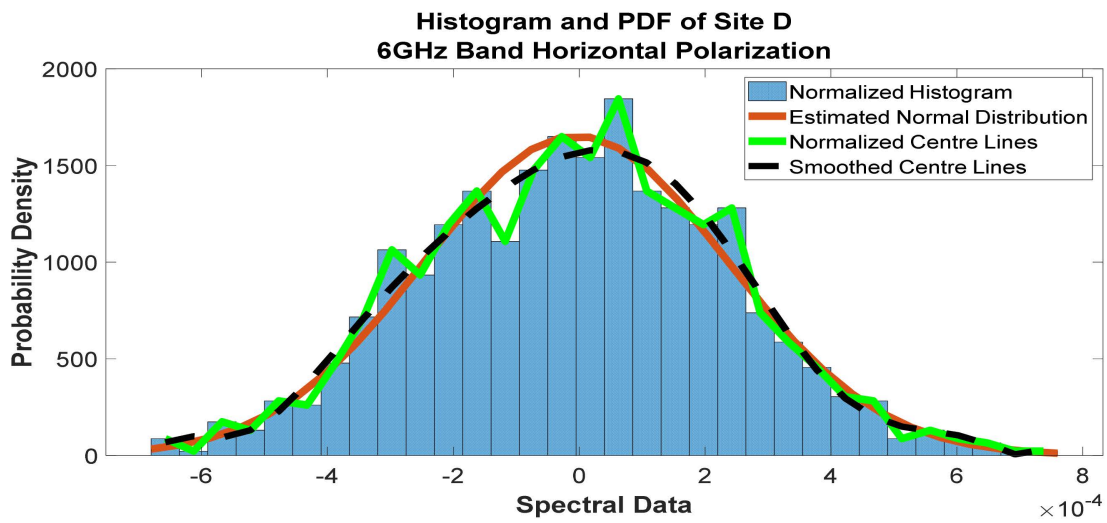


Figure 14. Histogram and PDF of the frequency scan for site D at 6 GHz horizontal polarization.

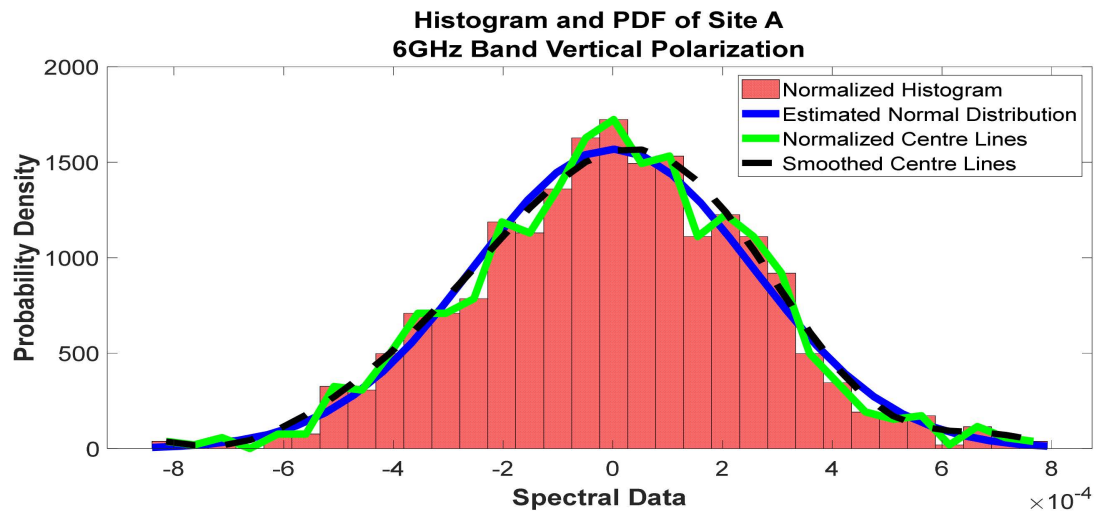


Figure 15. Histogram and PDF of the frequency scan for site A at 6 GHz vertical polarization.

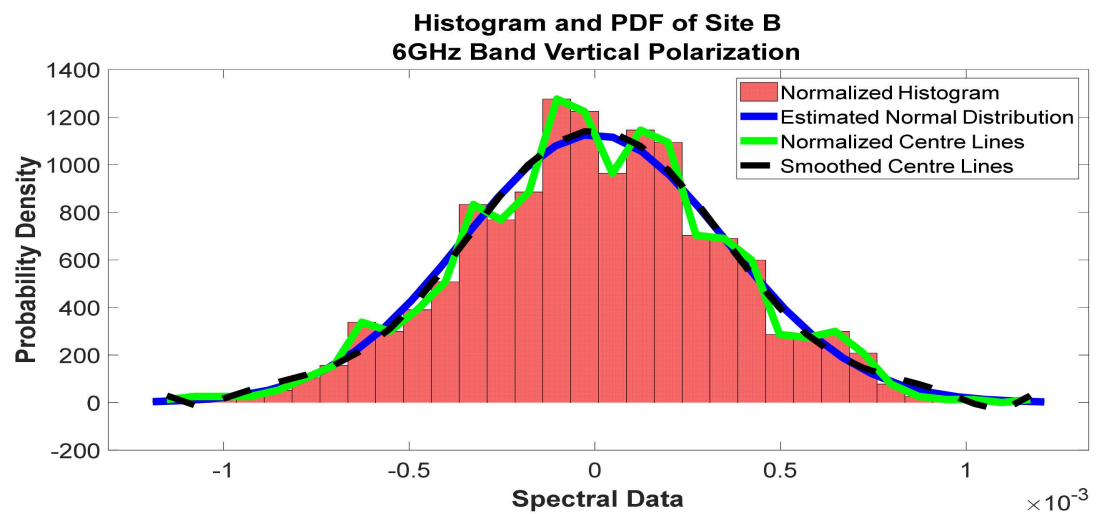


Figure 16. Histogram and PDF of the frequency scan for site B at 6 GHz vertical polarization.

Figure 17 reports the histogram and PDF of the frequency scan for site C at the 6 GHz vertical polarization. Figure 18 presents the histogram and PDF of the frequency scan for site D at the 6 GHz vertical polarization. Figure 19 gives the histogram and PDF of the frequency scan for site A at the 7 GHz horizontal polarization. Figure 20 illustrates the histogram and PDF of the frequency scan for site B at the 7 GHz horizontal polarization. Figure 21 elaborates on the histogram and PDF of the frequency scan for site C at the 7 GHz horizontal polarization. Figure 22 shows the histogram and PDF of the frequency scan for site D at the 7 GHz horizontal polarization. Figure 23 gives the histogram and PDF of the frequency scan for site A at the 7 GHz vertical polarization. Figure 24 reports the histogram and PDF of the frequency scan for site B at the 7 GHz vertical polarization. Figure 25 shows the histogram and PDF of the frequency scan for site C at the 7 GHz vertical polarization. Figure 26 depicts the histogram and PDF of the frequency scan for site D at the 7 GHz vertical polarization.

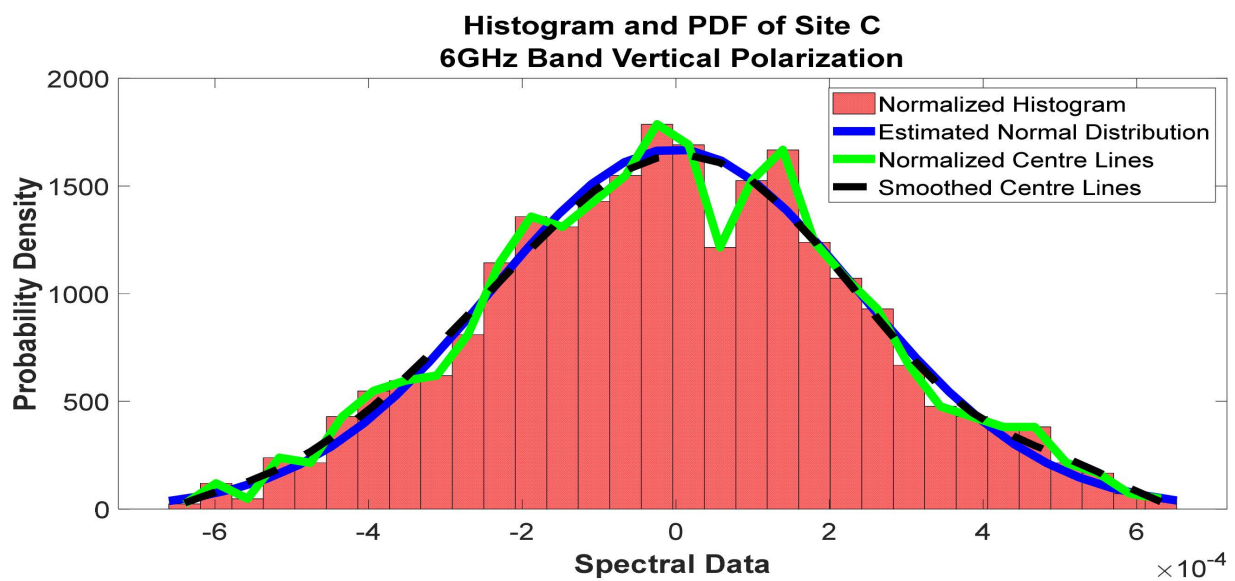


Figure 17. Histogram and PDF of the frequency scan for site C at 6 GHz vertical polarization.

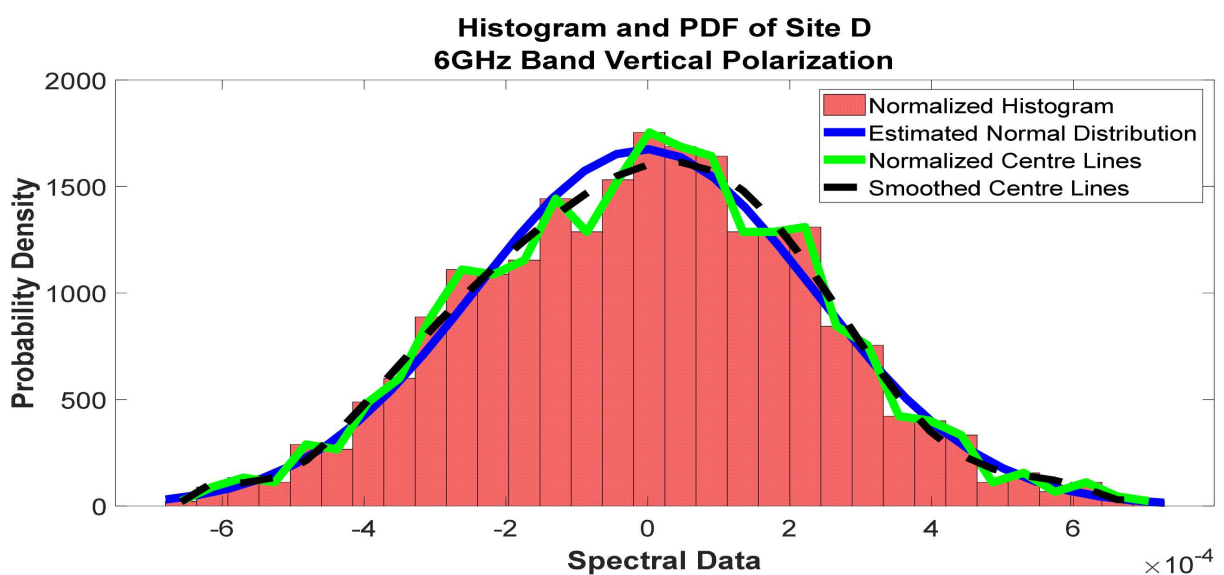


Figure 18. Histogram and PDF of the frequency scan for site D at 6 GHz vertical polarization.

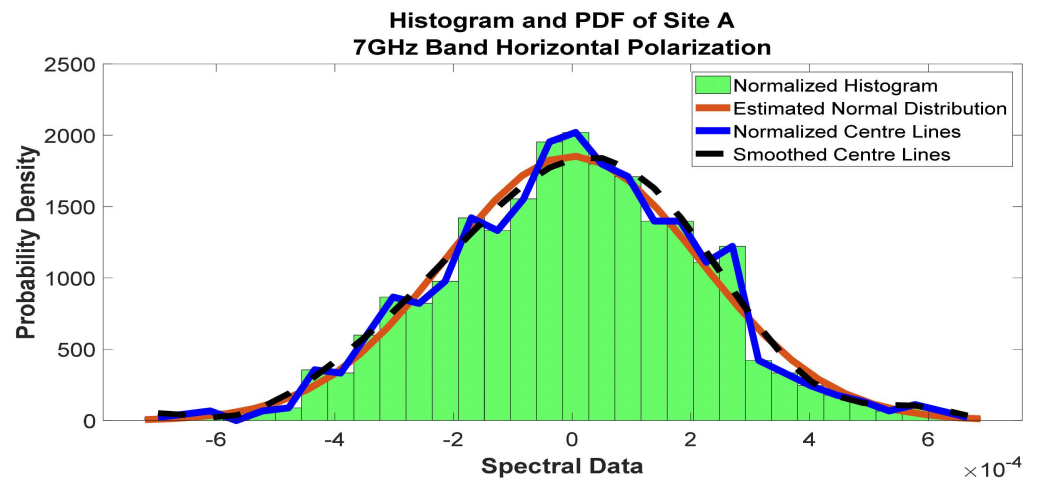


Figure 19. Histogram and PDF of the frequency scan for site A at 7 GHz horizontal polarization.

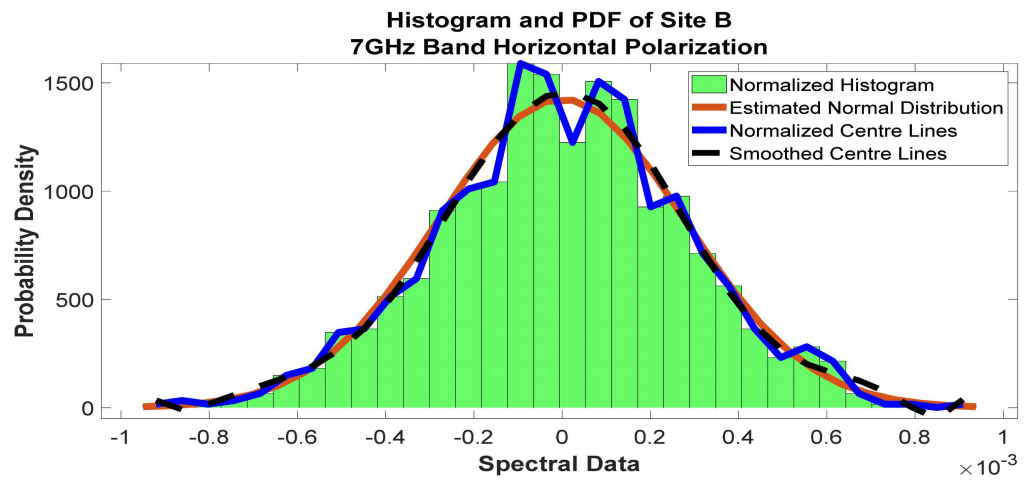


Figure 20. Histogram and PDF of the frequency scan for site B at 7 GHz horizontal polarization.

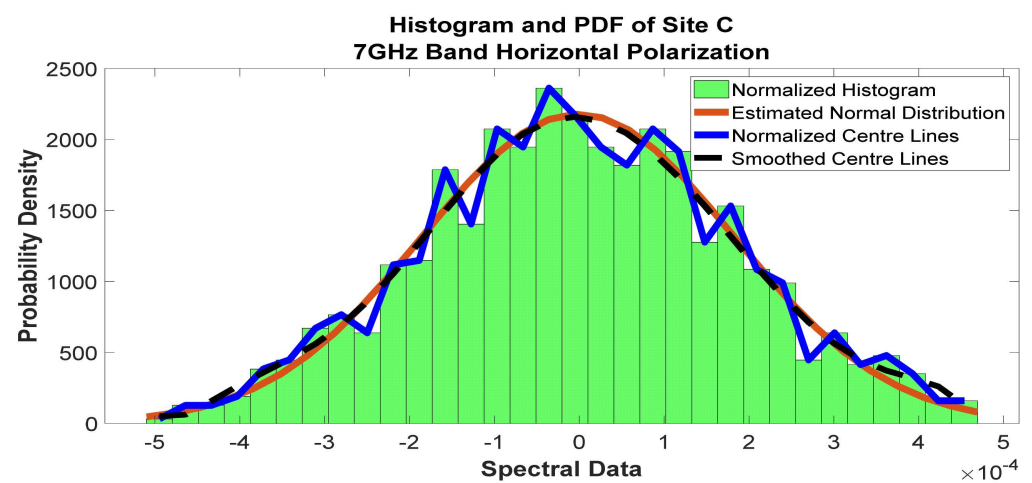


Figure 21. Histogram and PDF of the frequency scan for site C at 7 GHz horizontal polarization.

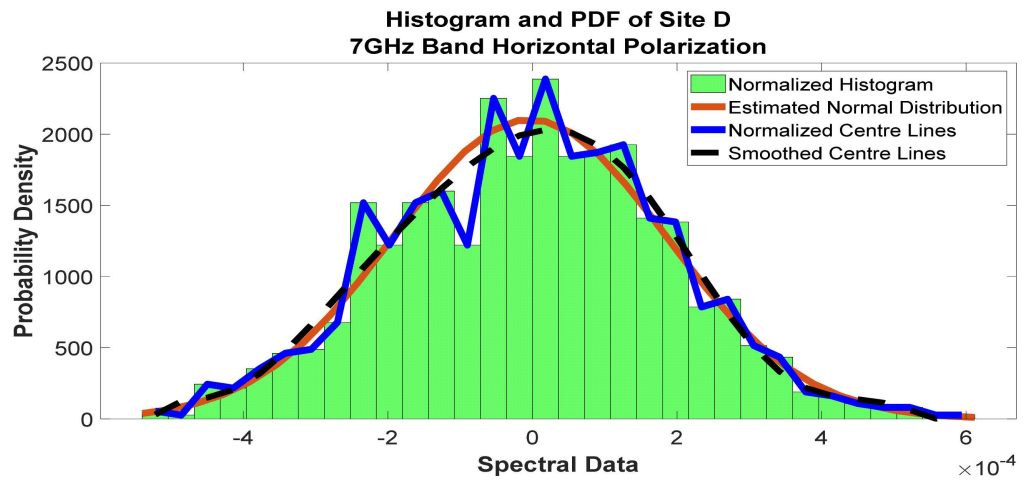


Figure 22. Histogram and PDF of the frequency scan for site D at 7 GHz horizontal polarization.

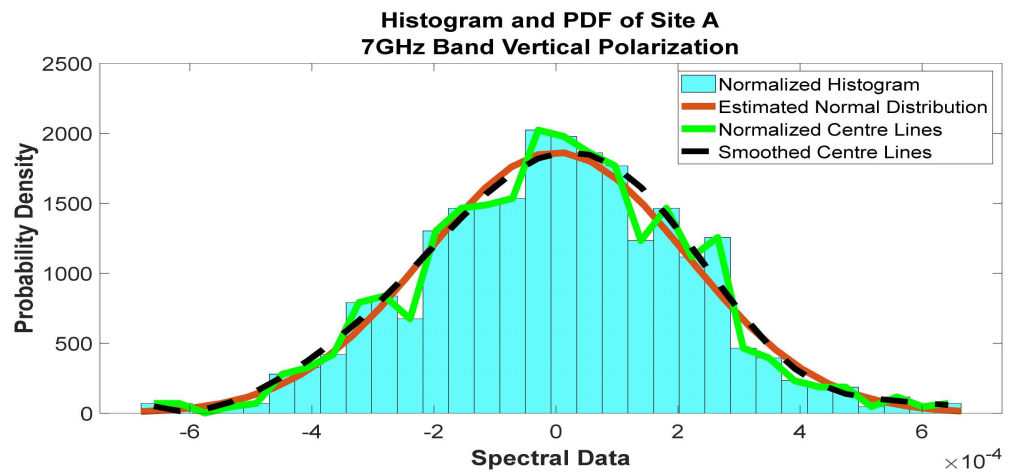


Figure 23. Histogram and PDF of the frequency scan for site A at 7 GHz vertical polarization.

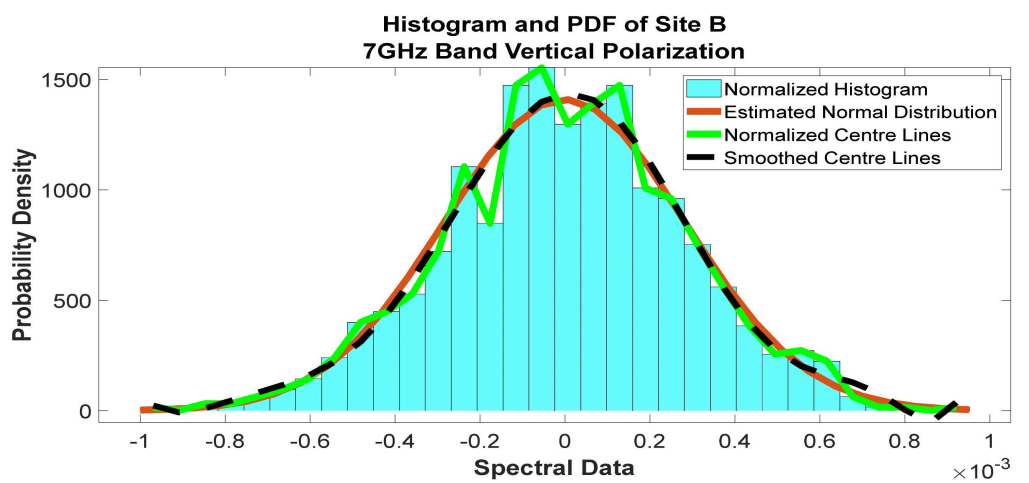


Figure 24. Histogram and PDF of the frequency scan for site B at 7 GHz vertical polarization.

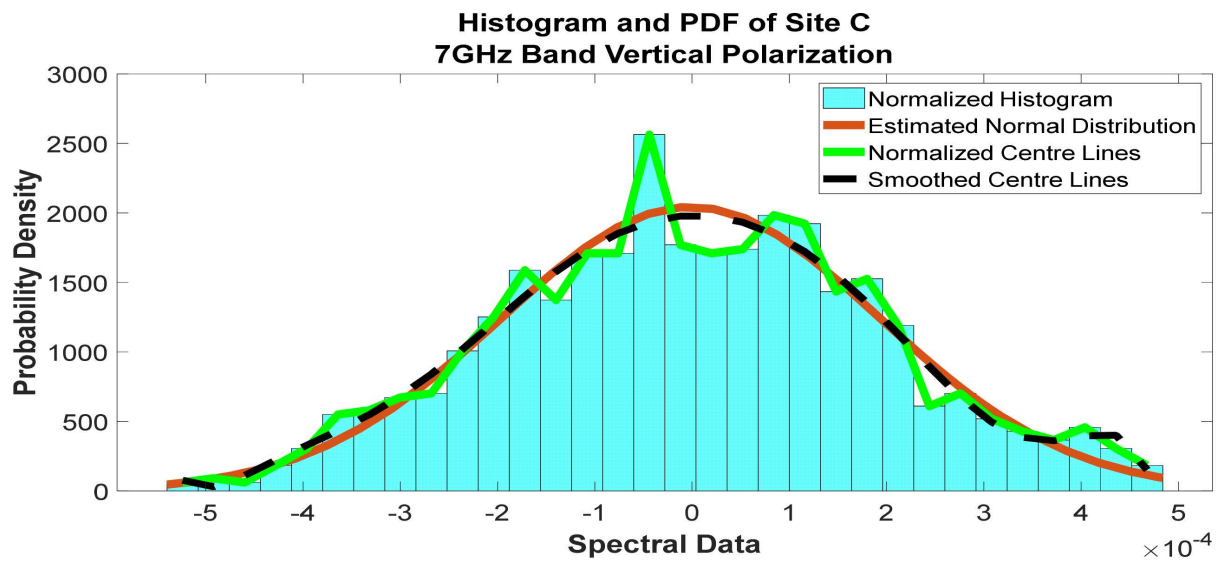


Figure 25. Histogram and PDF of the frequency scan for site C at 7 GHz vertical polarization.

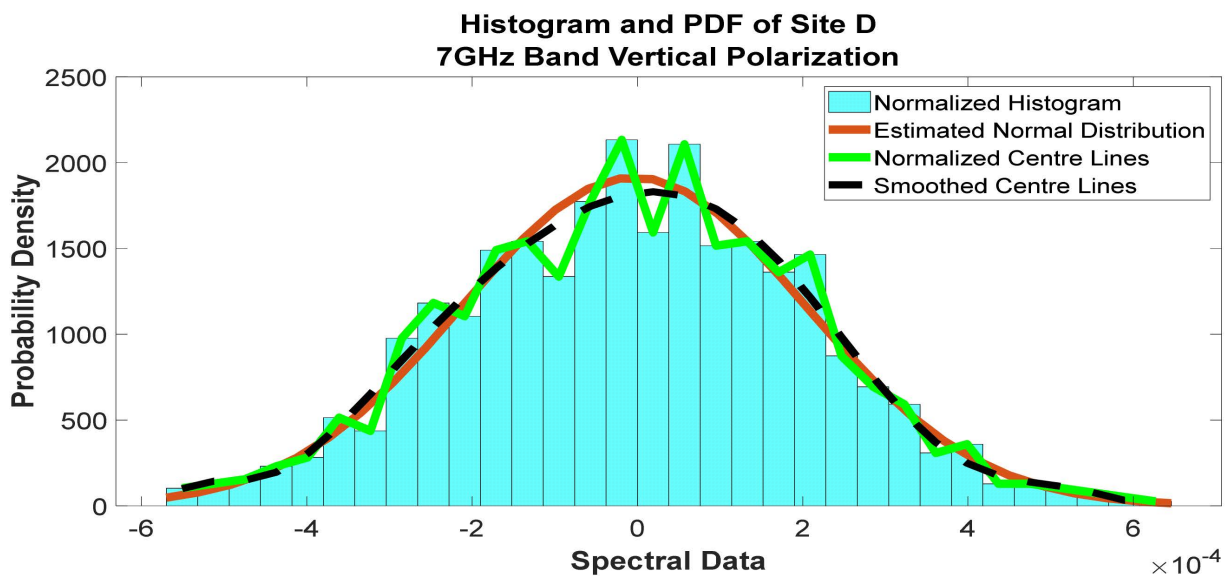


Figure 26. Histogram and PDF of the frequency scan for site D at 7 GHz vertical polarization.

Figure 27 illustrates the histogram and PDF of the frequency scan for site A at the 8 GHz horizontal polarization. Figure 28 gives the histogram and PDF of the frequency scan for site B at the 8 GHz horizontal polarization. Figure 29 shows the histogram and PDF of the frequency scan for site C at the 8 GHz horizontal polarization. Figure 30 gives the histogram and PDF of the frequency scan for site D at the 8 GHz horizontal polarization. Figure 31 elaborates on the histogram and PDF of the frequency scan for site A at the 8 GHz vertical polarization. Figure 32 gives the histogram and PDF of the frequency scan for site B at the 8 GHz vertical polarization. Figure 33 shows the histogram and PDF of the frequency scan for site C at the 8 GHz vertical polarization. Finally, Figure 34 presents the histogram and PDF of the frequency scan for site D at the 8 GHz vertical polarization.

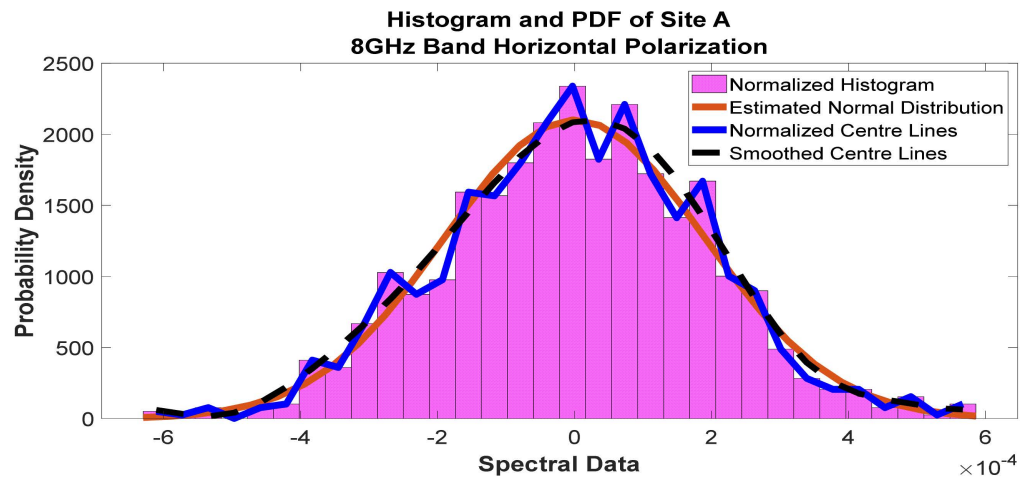


Figure 27. Histogram and PDF of the frequency scan for site A at 8 GHz horizontal polarization.

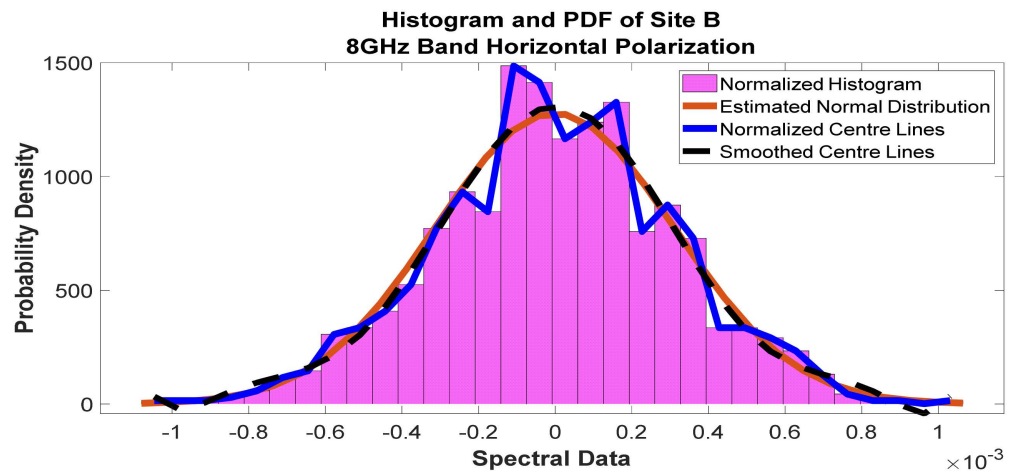


Figure 28. Histogram and PDF of the frequency scan for site B at 8 GHz horizontal polarization.

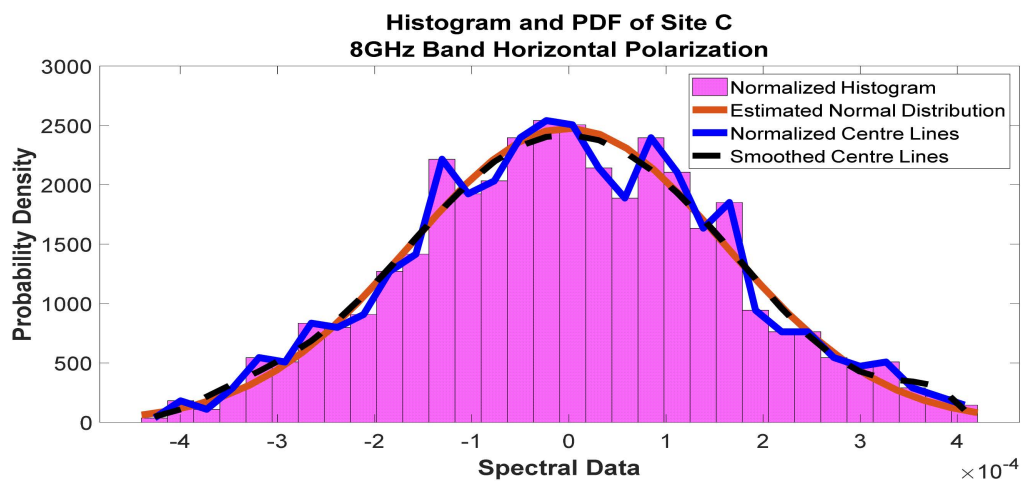


Figure 29. Histogram and PDF of the frequency scan for site C at 8 GHz horizontal polarization.

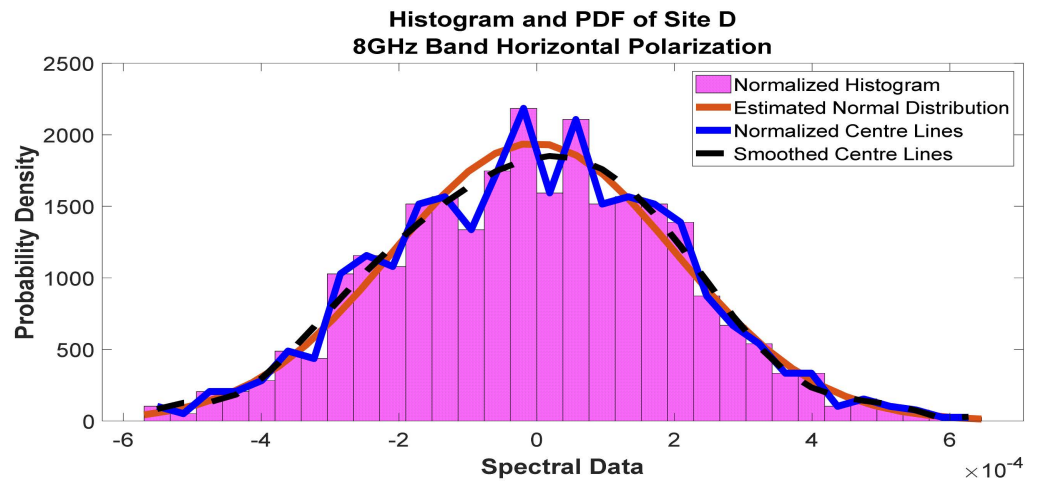


Figure 30. Histogram and PDF of the frequency scan for site D at 8 GHz horizontal polarization.

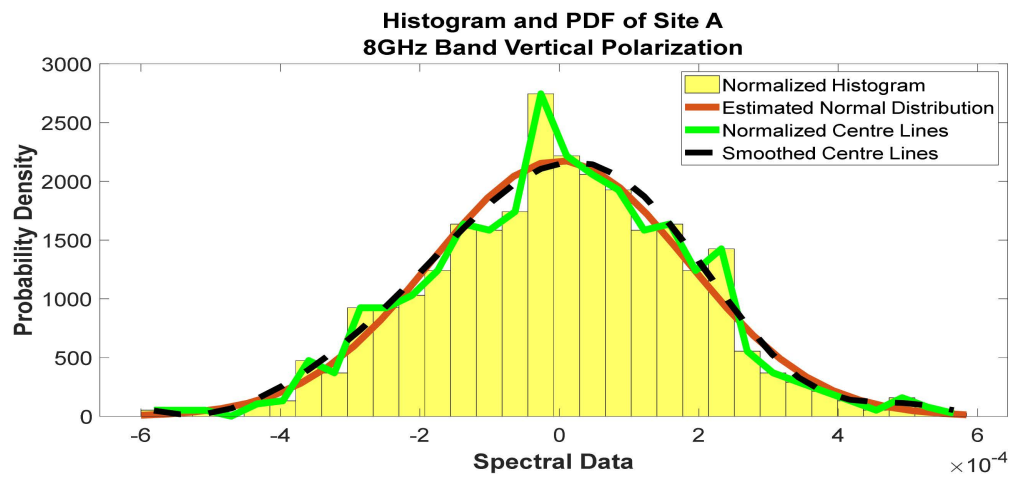


Figure 31. Histogram and PDF of the frequency scan for site A at 8 GHz vertical polarization.

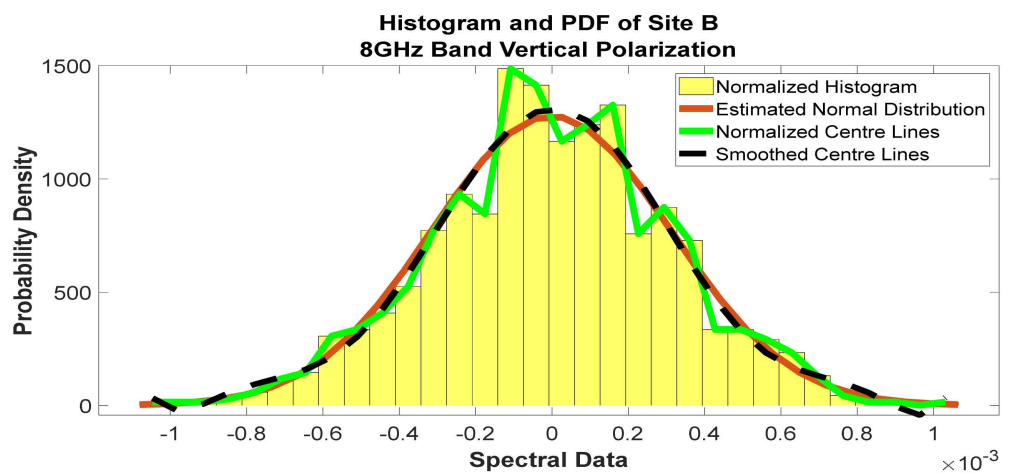


Figure 32. Histogram and PDF of the frequency scan for site B at 8 GHz vertical polarization.

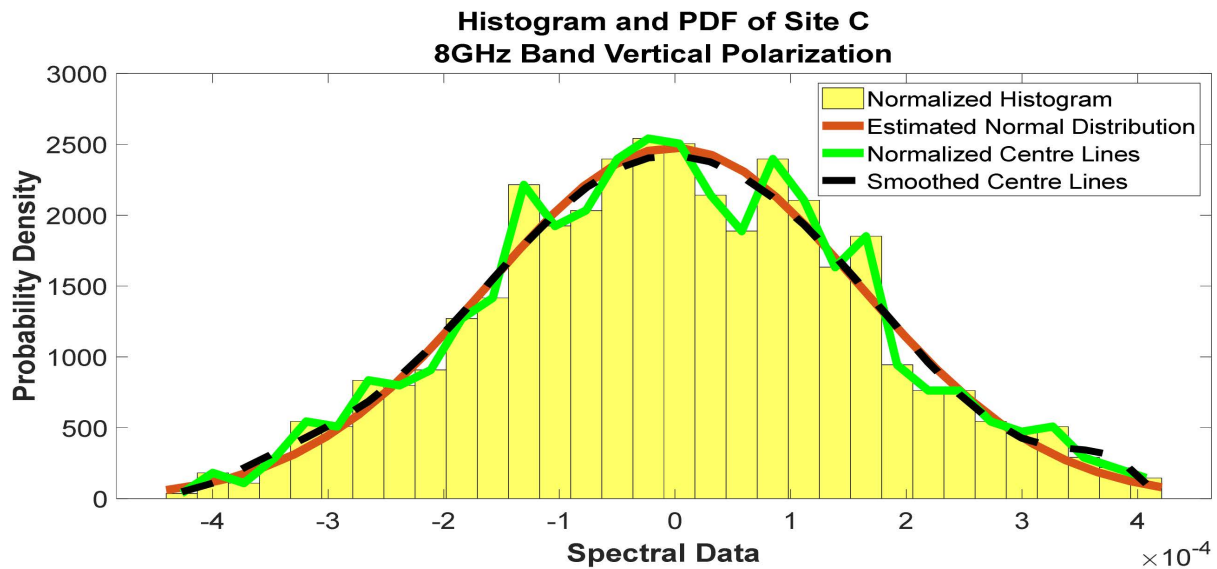


Figure 33. Histogram and PDF of the frequency scan for site C at 8 GHz vertical polarization.

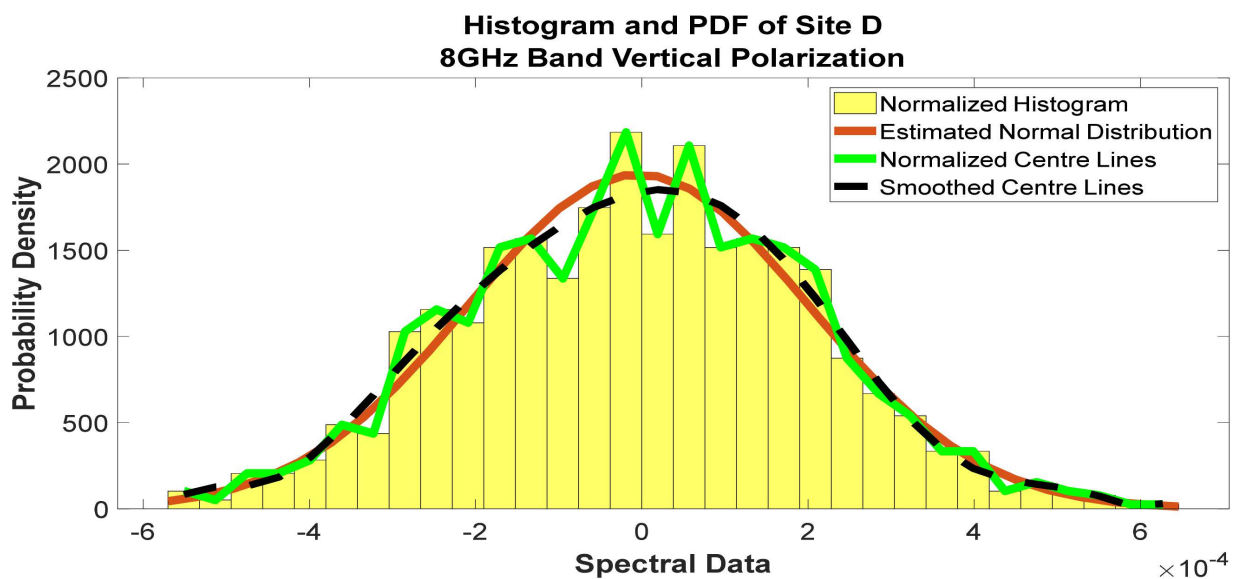


Figure 34. Histogram and PDF of the frequency scan for site D at 8 GHz vertical polarization.

4.3. Cumulative Distribution Function

The cumulative distribution functions (CDF) of the frequency scans for all sites at the 6 GHz, 7 GHz, and 8 GHz bands in the horizontal and vertical polarizations are given in Figures 35–40. Notably, Figure 35 shows the cumulative distribution functions of the frequency scans at the 6 GHz horizontal polarization for all sites. Figure 36 presents the cumulative distribution functions of the frequency scans for all of the sites at the 6 GHz vertical polarization. In Figure 37, the cumulative distribution functions of the frequency scans for all of the sites at the 7 GHz horizontal polarization are presented. Similarly, in Figure 38, the cumulative distribution functions of the frequency scans for all of the sites at the 7 GHz vertical polarization are reported. Figure 39 shows the cumulative distribution functions of the frequency scans for all of the sites at the 8 GHz horizontal polarization. Figure 40 elaborates on the cumulative distribution functions of the frequency scans for all of the sites at the 8 GHz vertical polarization.

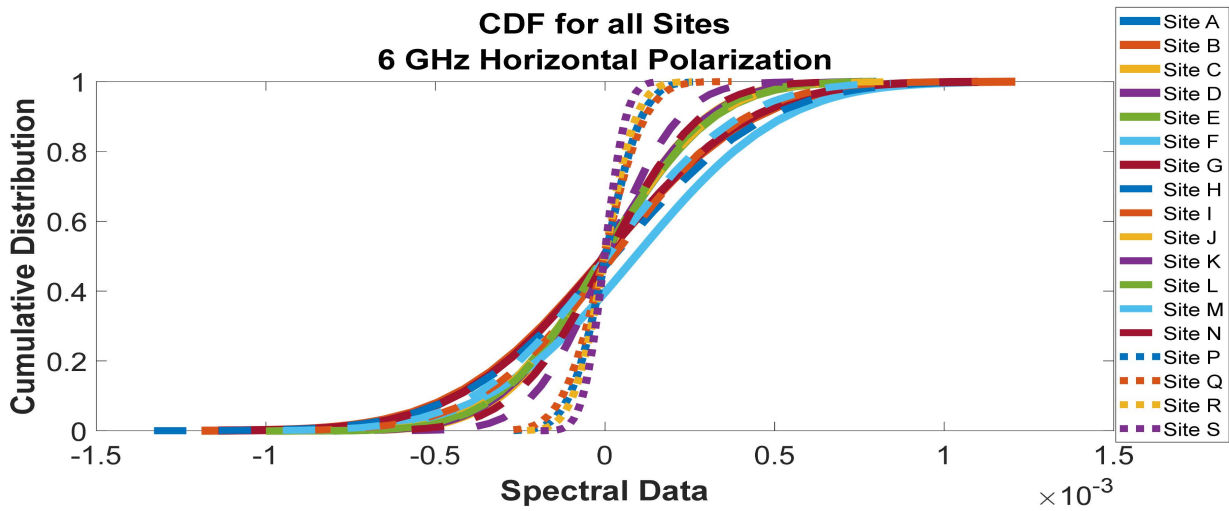


Figure 35. Cumulative distribution functions of frequency scan for all sites at 6 GHz horizontal polarization.

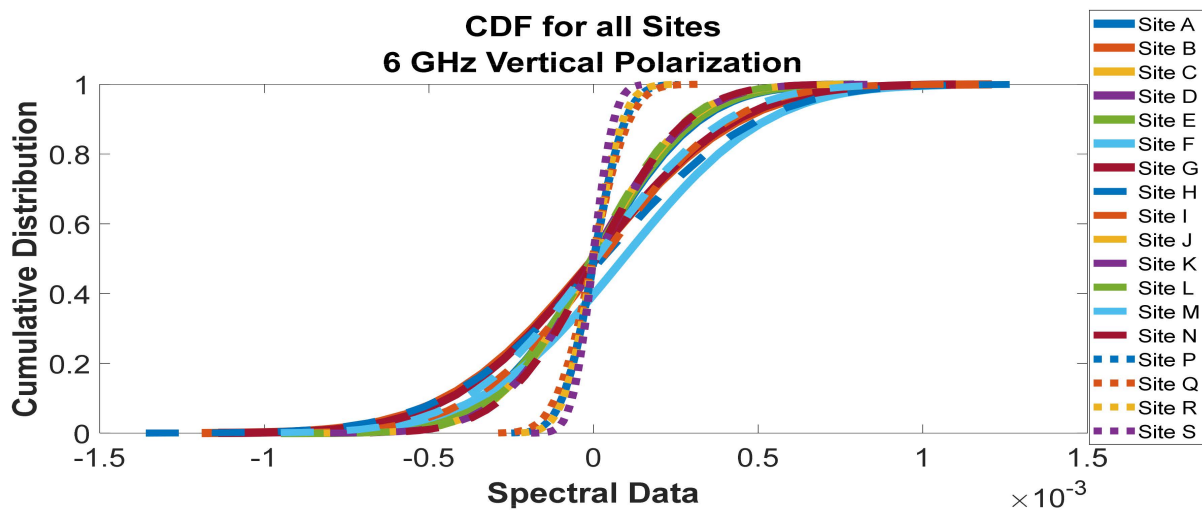


Figure 36. Cumulative distribution functions of frequency scan for all sites at 6 GHz vertical polarization.

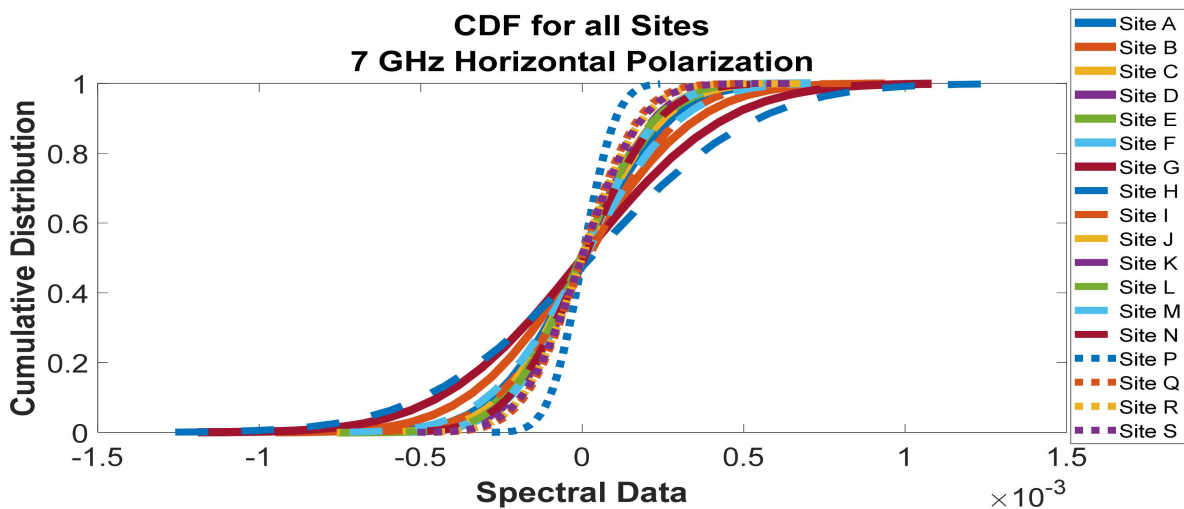


Figure 37. Cumulative distribution functions of frequency scan for all sites at 7 GHz horizontal polarization.

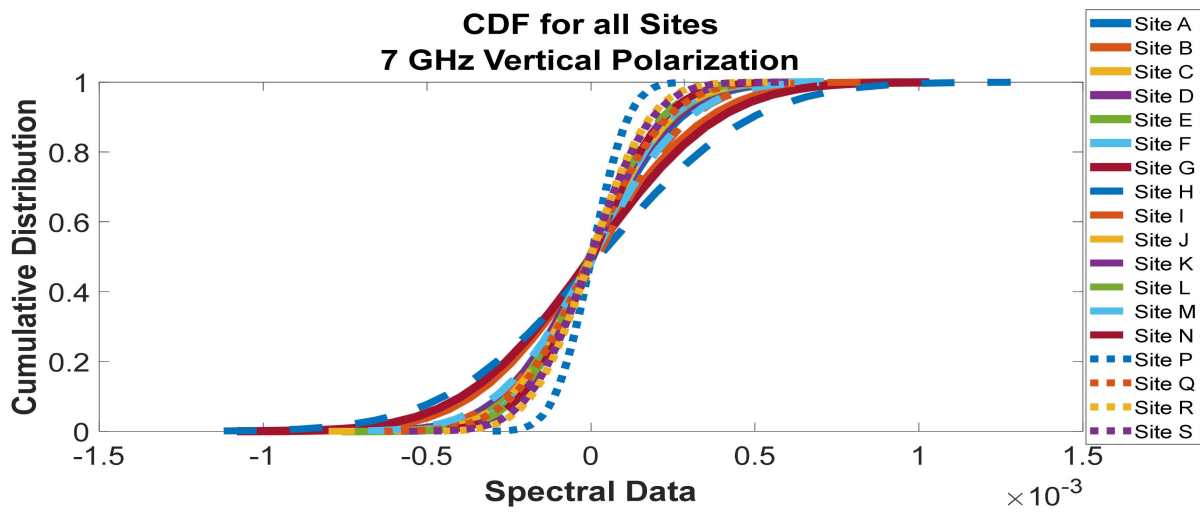


Figure 38. Cumulative distribution functions of frequency scan for all sites at 7 GHz vertical polarization.

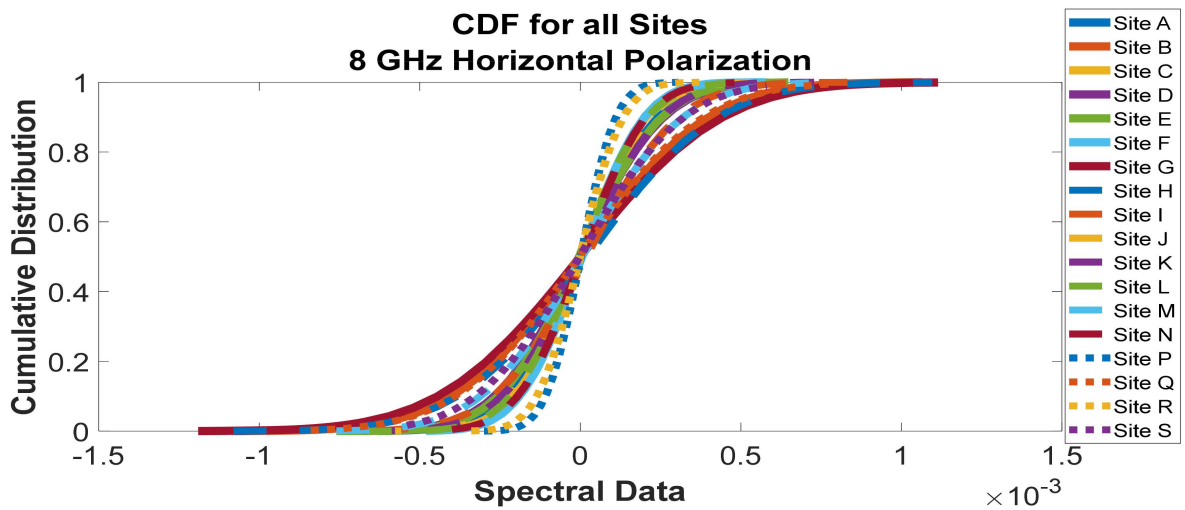


Figure 39. Cumulative distribution functions of frequency scan for all sites at 8 GHz horizontal polarization.

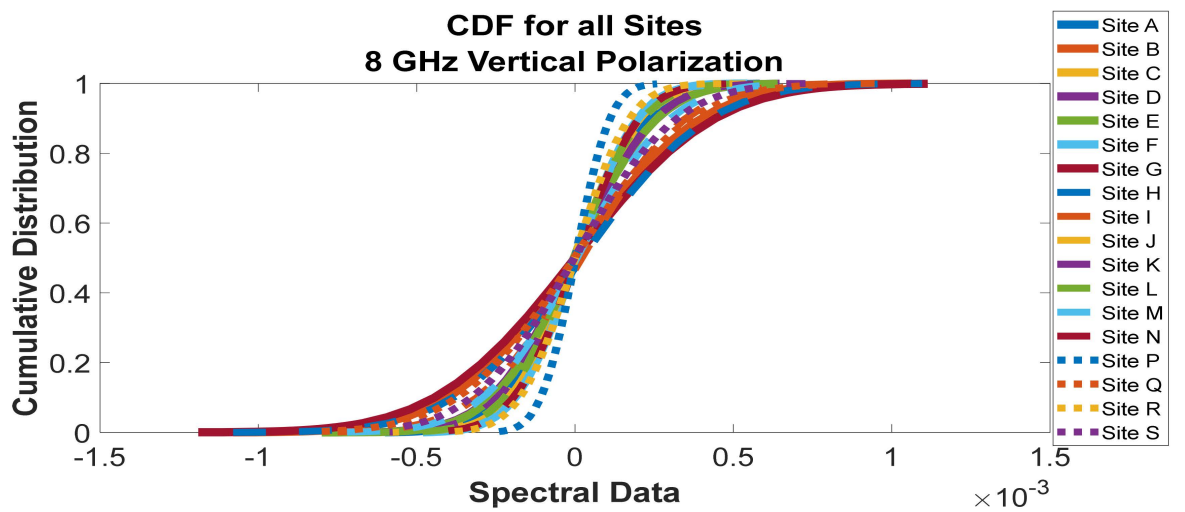


Figure 40. Cumulative distribution functions of frequency scan for all sites at 8 GHz vertical polarization.

4.4. Statistical Error Analysis

The statistical error analysis of the frequency scan measurements at 6 GHz, 7 GHz, and 8 GHz in the horizontal and vertical polarization is presented in this section. The errors include the mean absolute error (MAE), root mean squared error (RMSE), mean absolute percentage error (MAPE), relative absolute error (RAE), and the mean squared error (MSE) as presented in Tables 6–11. In particular, Table 6 shows the error analysis for the estimated normal distribution (Y) and the estimated fitness curve (F). The first five columns describe the error in the PDF, and the last five columns describe the errors in the fitness curve of the 6 GHz horizontal polarization. Table 7 presents the error analysis for the estimated normal distribution (Y) and the estimated fitness curve (F). The first five columns describe the error in the PDF, and the last five columns represent the errors in the fitness curve for 6 GHz vertical polarization. Table 8 gives the error analysis for the estimated normal distribution (Y) and the estimated fitness curve (F). The first five columns describe the error in the PDF, and the last five columns describe the errors in the fitness curve for 7 GHz horizontal polarization. Table 9 presents the error analysis for the estimated normal distribution (Y) and the estimated fitness curve (F). The first five columns describe the error in the PDF, and the last five columns describe the errors in the fitness curve for 7 GHz vertical polarization. Table 10 reports the error analysis for the estimated normal distribution (Y) and the estimated fitness curve (F). The first five columns describe the error in the PDF, and the last five columns describe the errors in the fitness curve for 8 GHz horizontal polarization. Finally, Table 11 gives the error analysis for the estimated normal distribution (Y) and the estimated fitness curve (F). The first five columns describe the error in the PDF, and the last five columns describe the errors in the fitness curve for the 8 GHz vertical polarization.

Table 6. Error analysis for the estimated normal distribution (Y) and the estimated fitness curve (F), where the first five columns describe the error in the PDF and the last five columns describe the errors in the fitness curve for the 6 GHz horizontal polarization.

Sites	MAE_Y	RMSE_Y	MAPE_Y	RAE_Y	MSE_Y($\times 10^4$)	MAE_F	RMSE_F	MAPE_F	RAE_F	MSE_F($\times 10^4$)
A	81.14	115.97	0.2716	0.1367	1.3450	85.64	111.81	0.3255	0.1318	1.2501
B	57.19	79.04	0.3929	0.1348	0.6246	61.30	78.57	1.5153	0.1340	0.6174
C	73.02	92.22	0.1887	0.0961	0.8505	60.48	77.62	0.1590	0.0809	0.6025
D	80.60	125.03	0.2365	0.1387	1.5633	75.92	107.03	0.2787	0.1187	1.1455
E	62.79	90.56	0.3388	0.1137	0.8201	61.05	86.49	1.2433	0.1086	0.7480
F	87.88	116.69	2.6438	0.1806	1.3612	65.16	86.52	1.6073	0.1339	0.7486
G	51.97	78.61	1.0338	0.1295	0.6177	46.00	59.56	2.4757	0.0981	0.3547
H	44.44	62.00	0.5683	0.1076	0.3844	41.97	59.37	0.4917	0.1031	0.3525
I	55.38	85.19	0.8604	0.1252	0.7257	55.44	82.70	1.6589	0.1215	0.6840
J	56.83	91.09	0.5348	0.1180	0.8296	50.58	76.64	1.4309	0.0993	0.5874
K	101.26	144.58	1.2996	0.1212	2.0902	87.15	134.37	0.9198	0.1126	1.8055
L	61.00	86.01	0.5199	0.1020	0.7398	56.78	80.17	1.4000	0.0951	0.6427
M	72.58	99.47	1.2024	0.1390	0.9892	61.46	89.07	1.7965	0.1245	0.7934
N	111.13	145.61	1.6398	0.1422	2.1200	100.35	135.57	2.3125	0.1324	1.8378
P	199.62	280.51	3.7499	0.1131	7.8677	180.88	248.04	3.5667	0.1000	6.1521
Q	146.20	201.68	1.6824	0.0941	4.0673	127.28	174.96	1.9093	0.0816	3.0610
R	253.38	410.28	0.9086	0.1446	16.8327	252.58	381.94	0.7003	0.1346	14.5876
S	372.28	568.43	13.6276	0.1373	32.3082	331.23	539.07	17.4459	0.1302	29.0599

4.5. Signal Denoising

The analyzed results showing the suppression of noise in the measured signal are presented in this section. The results of the measured signal before noise removal are presented earlier in Figures 5–10 of Section 4.2 in this paper. The signal waveforms after noise removal are given in Figures 41–46. Specifically, Figure 41 presents the 6 GHz horizontal polarization scan for all sites after denoising and applying the algorithm to all sites, including those without the potential to cause interference. Figure 42 shows the 6 GHz vertical polarization scan for all sites after denoising and applying the algorithm to all sites, including those without the potential to cause interference. Figure 43 depicts the

7 GHz horizontal polarization scan for all sites after denoising and applying the algorithm to all sites, including those without the potential to cause interference.

Table 7. Error analysis for the estimated normal distribution (Y) and the estimated fitness curve (F), where the first five columns describe the error in the PDF and the last five columns describe the errors in the fitness curve for the 6 GHz vertical polarization.

Sites	MAE_Y	RMSE_Y	MAPE_Y	RAE_Y	MSE_Y($\times 10^4$)	MAE_F	RMSE_F	MAPE_F	RAE_F	MSE_F($\times 10^4$)
A	80.63	98.93	1.6353	0.1190	0.9784	69.27	91.10	1.6878	0.1096	0.8300
B	58.34	80.19	0.4142	0.1373	0.6431	62.16	79.74	1.5288	0.1365	0.6359
C	81.31	115.62	0.1963	0.1221	1.3369	68.73	105.55	0.1750	0.1114	1.1140
D	76.52	105.09	0.1930	0.1148	1.1045	66.75	83.65	0.1789	0.0913	0.6996
E	80.32	123.98	1.0729	0.1500	1.5372	79.08	120.37	3.9053	0.1457	1.4489
F	87.82	116.67	2.6438	0.1806	1.3612	65.16	86.52	1.6073	0.1339	0.7486
G	51.91	78.59	1.0338	0.1295	0.6177	46.00	59.56	2.4757	0.0981	0.3547
H	44.46	66.01	0.9776	0.1222	0.4358	45.74	64.17	2.4783	0.1188	0.4118
I	55.32	85.19	0.8604	0.1252	0.7257	55.44	82.70	1.6589	0.1215	0.6840
J	58.53	99.68	0.6650	0.1168	0.9936	48.73	81.89	1.6793	0.0959	0.6706
K	58.61	97.20	0.4869	0.1106	0.9447	57.23	85.82	1.3762	0.0977	0.7365
L	62.25	89.44	0.5839	0.0996	0.7999	54.84	85.03	1.3270	0.0947	0.7229
M	68.71	91.35	0.2786	0.1297	0.8345	57.31	81.01	0.2522	0.1150	0.6562
N	103.15	139.66	0.2687	0.1373	1.9505	98.50	129.72	0.2840	0.1276	1.6828
P	247.14	313.64	8.2762	0.1143	9.8368	212.26	288.36	6.4423	0.1050	8.3149
Q	168.73	240.67	1.8458	0.1038	5.7923	165.49	232.12	3.5493	0.1001	5.3881
R	266.11	395.94	3.4193	0.1353	15.6767	252.96	361.40	5.1626	0.1235	13.0610
S	372.16	568.40	13.6276	0.1373	32.3082	331.23	539.07	17.4459	0.1302	29.0599

Table 8. Error analysis for the estimated normal distribution (Y) and the estimated fitness curve (F), where the first five columns describe the error in the PDF and the last five columns describe the errors in the fitness curve for the 7 GHz horizontal polarization.

Sites	MAE_Y	RMSE_Y	MAPE_Y	RAE_Y	MSE_Y($\times 10^4$)	MAE_F	RMSE_F	MAPE_F	RAE_F	MSE_F($\times 10^4$)
A	88.86	123.88	1.6733	0.1273	1.5343	84.91	114.43	1.3897	0.1176	1.3094
B	63.50	93.42	0.5082	0.1263	0.8728	64.23	90.55	1.9711	0.1224	0.8199
C	139.01	163.20	0.2052	0.1301	2.6635	121.88	151.59	0.1871	0.1208	2.2981
D	121.05	194.92	0.2324	0.1704	3.7995	119.11	179.78	0.3105	0.1572	3.2320
E	83.62	129.86	0.3822	0.1245	1.6864	80.01	124.56	1.3817	0.1194	1.5516
F	88.76	126.17	2.1202	0.1125	1.5918	83.92	115.31	2.7276	0.1029	1.3297
G	53.72	73.85	0.2935	0.1230	0.5454	42.75	59.48	0.3441	0.0991	0.3538
H	65.97	91.76	0.6539	0.1761	0.8420	59.84	85.33	0.8471	0.1638	0.7281
I	69.78	108.30	0.6132	0.1164	1.1729	68.74	104.69	1.2885	0.1125	1.0960
J	77.78	124.09	1.3754	0.1247	1.5399	68.80	109.20	1.2062	0.1097	1.1924
K	96.09	145.19	0.3791	0.1204	2.1079	90.72	136.53	0.3677	0.1132	1.8642
L	85.00	131.92	0.2614	0.1168	1.7402	77.06	125.75	0.9510	0.1113	1.5814
M	87.34	120.57	0.2474	0.1293	1.4536	74.72	105.86	0.1277	0.1136	1.1206
N	154.43	225.09	0.7704	0.1117	1.7681	84.69	113.54	0.6018	0.0954	1.2892
P	201.75	277.06	2.1308	0.1061	7.6762	187.23	253.44	5.1209	0.0970	6.4231
Q	166.47	225.80	0.3395	0.1480	5.0985	118.88	148.11	0.3891	0.0971	2.1937
R	128.10	207.16	1.0163	0.1511	4.2915	127.68	184.76	8.5567	0.1347	3.4138
S	142.50	207.85	0.3534	0.1478	4.3201	94.50	123.70	0.5539	0.0880	1.5303

Table 9. Error analysis for the estimated normal distribution (Y) and the estimated fitness curve (F), where the first five columns describe the error in the PDF and the last five columns describe the errors in the fitness curve for the 7 GHz vertical polarization.

Sites	MAE_Y	RMSE_Y	MAPE_Y	RAE_Y	MSE_Y($\times 10^4$)	MAE_F	RMSE_F	MAPE_F	RAE_F	MSE_F($\times 10^4$)
A	108.18	142.39	1.5030	0.1420	2.0274	95.00	136.67	1.1399	0.1363	1.8679
B	61.38	94.26	0.6658	0.1304	0.8884	61.13	91.73	2.3281	0.1269	0.8414
C	141.95	185.35	0.2037	0.1556	3.4356	114.28	167.03	0.1647	0.1402	2.7898
D	105.99	153.82	0.1974	0.1454	2.3661	97.77	138.78	0.1419	0.1312	1.9260
E	83.62	129.86	0.3822	0.1245	1.6864	80.01	124.56	1.3817	0.1194	1.5516
F	109.64	163.02	2.3367	0.1476	2.6574	102.76	154.54	1.8779	0.1399	2.3883
G	51.63	74.25	1.7267	0.1124	0.5513	42.60	59.40	2.4694	0.0899	0.3528
H	57.21	83.98	0.4309	0.1455	0.7053	53.87	77.41	0.7717	0.1341	0.5993
I	68.41	107.53	0.6170	0.1156	1.1562	67.35	103.87	1.3269	0.1117	1.0789
J	90.03	130.83	1.2474	0.1292	1.7116	82.25	112.75	4.0385	0.1114	1.2712
K	77.79	101.39	0.7099	0.0870	1.0279	62.45	88.98	1.3740	0.0764	0.7918
L	71.61	108.77	0.5949	0.0933	1.1830	61.04	100.15	1.6584	0.0859	1.0031
M	108.72	139.61	2.3822	0.1479	1.9490	95.48	129.26	1.9073	0.1370	1.6708
N	159.36	207.55	0.2529	0.1586	4.3076	144.93	193.89	0.2773	0.1482	3.7595
P	218.98	294.38	1.8206	0.1229	8.6661	181.85	248.85	2.0382	0.1039	6.1929
Q	202.87	278.79	0.7323	0.2286	7.7722	136.76	175.85	3.3330	0.1442	3.0923
R	125.07	198.27	1.8680	0.1388	3.9312	113.09	140.29	8.6216	0.0982	1.9681
S	115.87	177.36	0.3512	0.1287	3.1458	95.18	122.80	1.1084	0.0891	1.5081

Table 10. Error analysis for the estimated normal distribution (Y) and the estimated fitness curve (F), where the first five columns describe the error in the PDF and the last five columns describe the errors in the fitness curve for the 8 GHz horizontal polarization.

Sites	MAE_Y	RMSE_Y	MAPE_Y	RAE_Y	MSE_Y($\times 10^4$)	MAE_F	RMSE_F	MAPE_F	RAE_F	MSE_F($\times 10^4$)
A	109.19	147.68	1.9333	0.1324	2.1811	110.38	137.71	1.5699	0.1235	1.8965
B	65.45	101.13	0.4435	0.1530	1.0227	67.62	99.75	1.8451	0.1509	0.9949
C	140.63	187.71	0.2004	0.1316	3.5235	133.53	172.79	0.1776	0.1212	2.9858
D	113.30	159.85	0.2116	0.1501	2.5551	100.71	141.64	0.1991	0.1330	2.0063
E	65.30	89.61	0.5164	0.0881	0.8030	61.07	81.71	2.0553	0.0804	0.6677
F	97.68	140.19	2.9085	0.1053	1.9654	73.39	127.29	3.1654	0.0956	1.6202
G	52.49	81.26	0.6503	0.1364	0.6603	50.70	70.61	0.8466	0.1185	0.4986
H	44.87	63.51	0.9339	0.0984	0.4034	47.02	61.46	2.0541	0.0952	0.3778
I	69.72	108.35	0.6201	0.1164	1.1740	68.74	104.69	1.2885	0.1125	1.0960
J	92.98	141.37	1.4869	0.1223	1.9984	77.45	125.94	2.9319	0.1089	1.5860
K	80.52	112.85	0.6384	0.1108	1.2736	76.34	99.59	1.6692	0.0977	0.9918
L	71.71	98.07	0.6084	0.0803	0.9617	60.21	84.86	1.8345	0.0695	0.7201
M	97.75	127.04	1.6089	0.1438	1.6140	83.54	114.00	0.7577	0.1291	1.2996
N	170.86	214.53	0.3151	0.1488	4.6025	168.42	203.31	0.3636	0.1410	4.1334
P	183.42	247.86	4.1610	0.1063	6.1437	174.72	239.04	6.4273	0.1025	5.7140
Q	95.49	139.85	1.5953	0.1873	1.9559	75.38	93.64	1.3522	0.1254	0.8769
R	181.96	249.46	4.0376	0.1282	6.2231	165.64	222.02	2.8758	0.1141	4.9292
S	301.65	378.08	0.4737	0.3764	14.2947	108.31	131.26	0.2279	0.1307	1.7228

Additionally, Figure 44 reports the 7 GHz vertical polarization scan for all sites after denoising and applying the algorithm to all sites, including those without the potential to cause interference. Figure 45 presents the 8 GHz horizontal polarization scan for all sites after denoising and applying the algorithm to all sites, including those without the potential to cause interference. Finally, Figure 46 gives the 8 GHz vertical polarization scan for all sites after denoising and applying the algorithm to all sites, including those without the potential to cause interference.

Table 11. Error analysis for the estimated normal distribution (Y) and the estimated fitness curve (F), where the first five columns describe the error in the PDF and the last five columns describe the errors in the fitness curve for the 8 GHz vertical polarization.

Sites	MAE_Y	RMSE_Y	MAPE_Y	RAE_Y	MSE_Y($\times 10^4$)	MAE_F	RMSE_F	MAPE_F	RAE_F	MSE_F($\times 10^4$)
A	115.78	181.57	2.2462	0.1572	3.2967	118.23	175.86	2.3627	0.1522	3.0927
B	65.45	101.13	0.4435	0.1530	1.0227	67.62	99.75	1.8451	0.1509	0.9949
C	140.63	187.71	0.2004	0.1316	3.5235	133.53	172.79	0.1776	0.1212	2.9858
D	113.30	159.85	0.2116	0.1501	2.5551	100.71	141.64	0.1991	0.1330	2.0063
E	81.68	115.79	0.3681	0.1164	1.3406	78.17	110.99	1.4093	0.1116	1.2318
F	140.95	201.42	4.2578	0.1482	4.0571	131.51	190.46	4.5442	0.1401	3.6275
G	52.49	81.26	0.6503	0.1364	0.6603	50.70	70.61	0.8466	0.1185	0.4986
H	44.87	63.51	0.9339	0.0984	0.4034	47.02	61.46	2.0541	0.0952	0.3778
I	57.16	79.91	0.5718	0.0987	0.6385	56.11	75.85	0.9910	0.0937	0.5754
J	92.98	141.37	1.4869	0.1223	1.9984	77.45	125.94	2.9319	0.1089	1.5860
K	80.52	112.85	0.6384	0.1108	1.2736	76.34	99.59	1.6692	0.0977	0.9918
L	85.99	121.67	0.7480	0.1019	1.4805	81.68	116.84	1.8264	0.0979	1.3652
M	89.52	119.15	0.2871	0.1269	1.4196	75.05	103.65	0.3221	0.1104	1.0743
N	159.08	212.35	0.2806	0.1468	4.5092	156.47	200.03	0.3152	0.1383	4.0014
P	239.54	312.41	0.2388	0.1209	9.7603	229.50	282.91	0.2374	0.1095	8.0038
Q	113.23	139.68	1.7515	0.1787	1.9511	88.54	108.79	2.2600	0.1392	1.1836
R	129.17	207.21	1.6191	0.1344	4.2937	120.26	179.28	1.2545	0.1163	3.2140
S	301.65	378.08	0.4737	0.3764	14.2947	108.31	131.26	0.2279	0.1307	1.7228

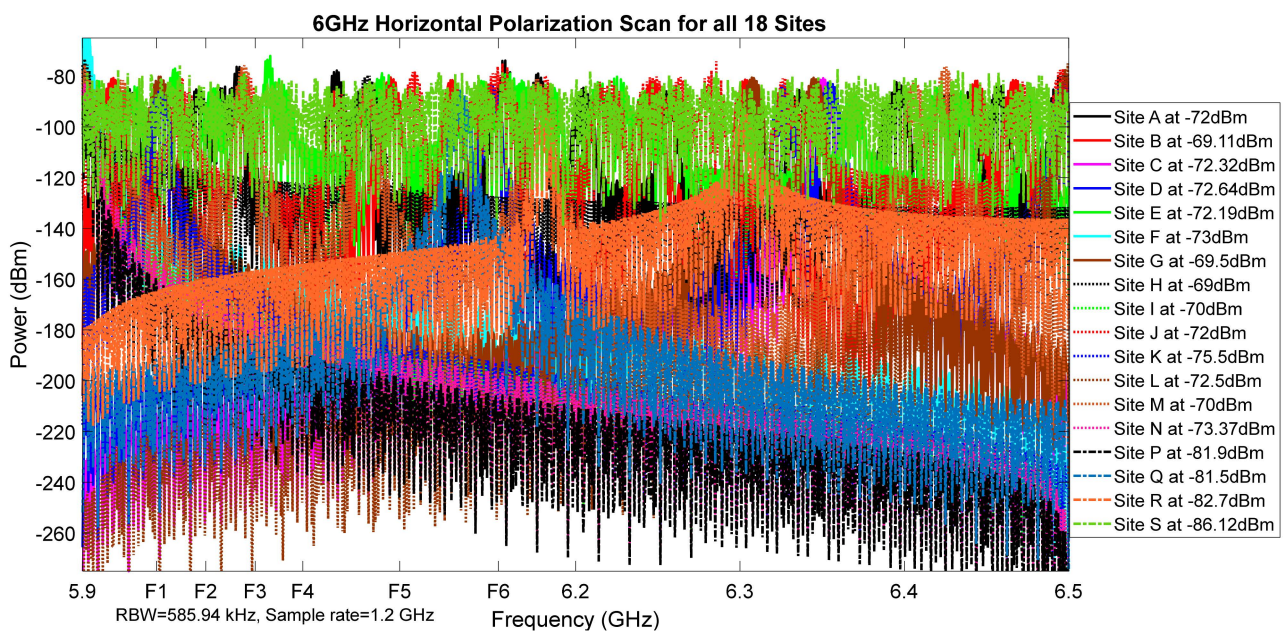


Figure 41. The 6 GHz horizontal polarization scan for all sites after denoising and applying the algorithm to all sites, including those without the potential to cause interference.

4.6. Comparison of the Signal before and after Denoising

This section compares the histogram and probability density function (PDF) of the frequency scan signals obtained before and after denoising, as shown in Figures 47–54. In particular, Figure 47 gives the histogram and PDF of the site E signals collected at the 6 GHz band horizontal polarization. Figure 48 presents the histogram and PDF of the denoised site E signals at the 6 GHz band horizontal polarization. Figure 49 shows the histogram and PDF of the actual site F signals at the 6 GHz band horizontal polarization. Similarly, Figure 50 depicts the histogram and PDF of the denoised site F signals at the 6 GHz band horizontal polarization. Figure 51 gives the histogram and PDF of the site I signal at the 6 GHz band horizontal polarization in the same vein.

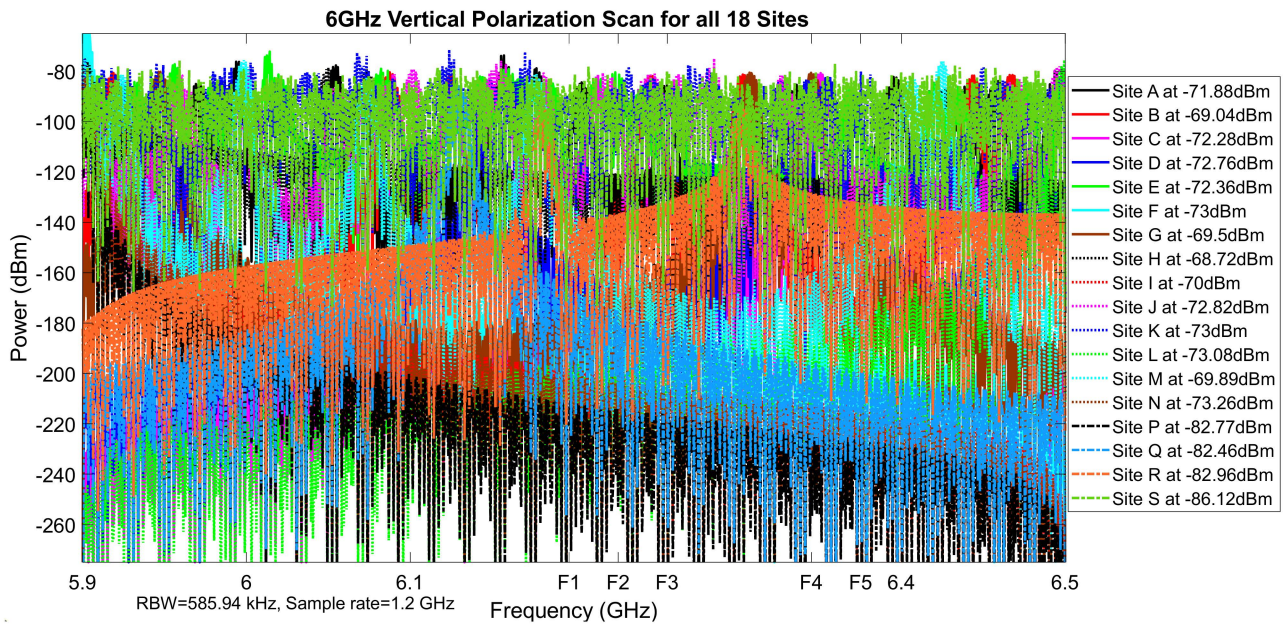


Figure 42. The 6 GHz vertical polarization scan for all sites after denoising and applying the algorithm to all sites, including those without the potential to cause interference.

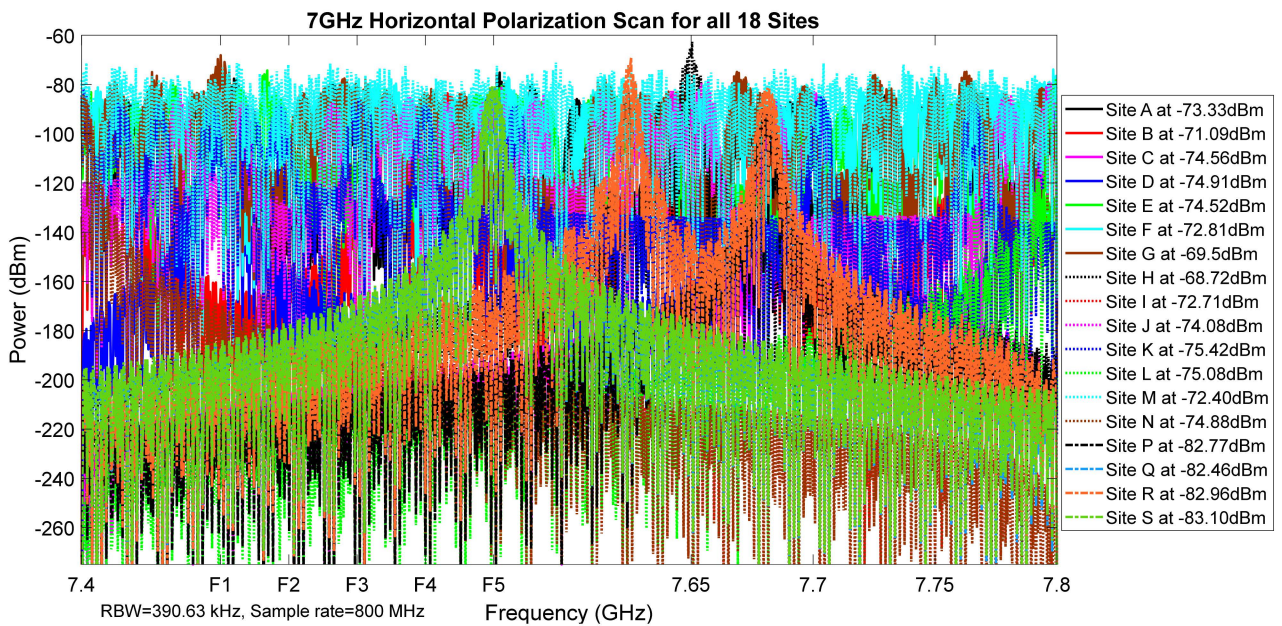


Figure 43. The 7 GHz horizontal polarization scan for all sites after denoising and applying the algorithm to all sites, including those without the potential to cause interference.

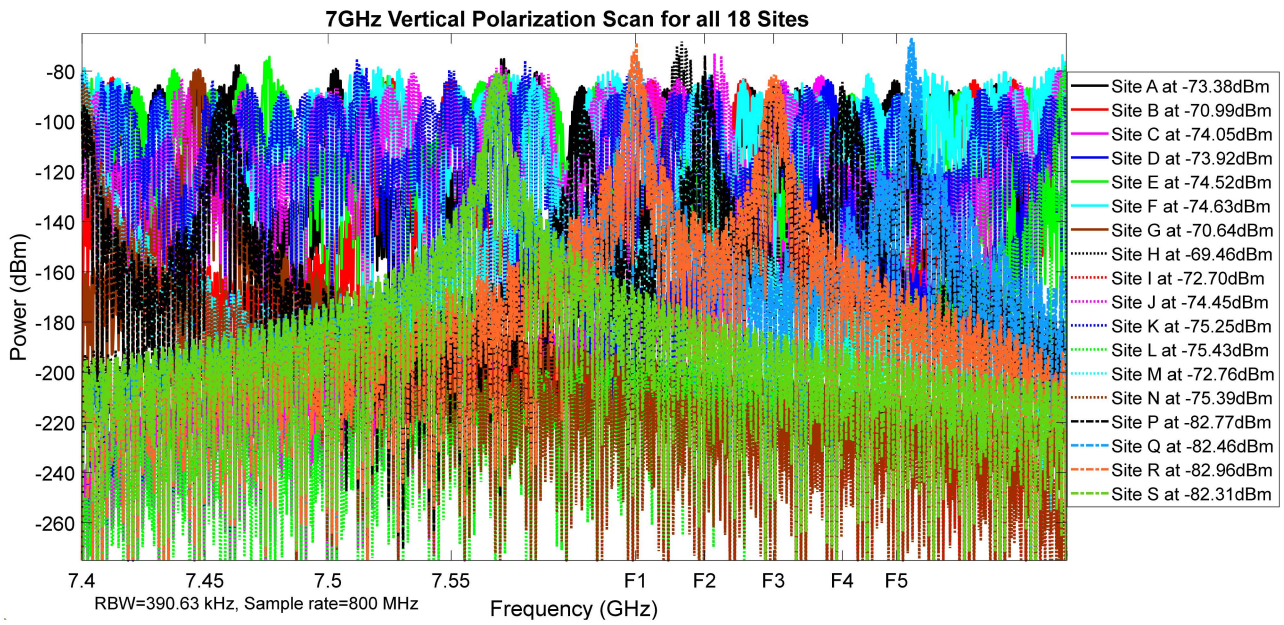


Figure 44. The 7 GHz vertical polarization scan for all sites after denoising and applying the algorithm to all sites, including those without the potential to cause interference.

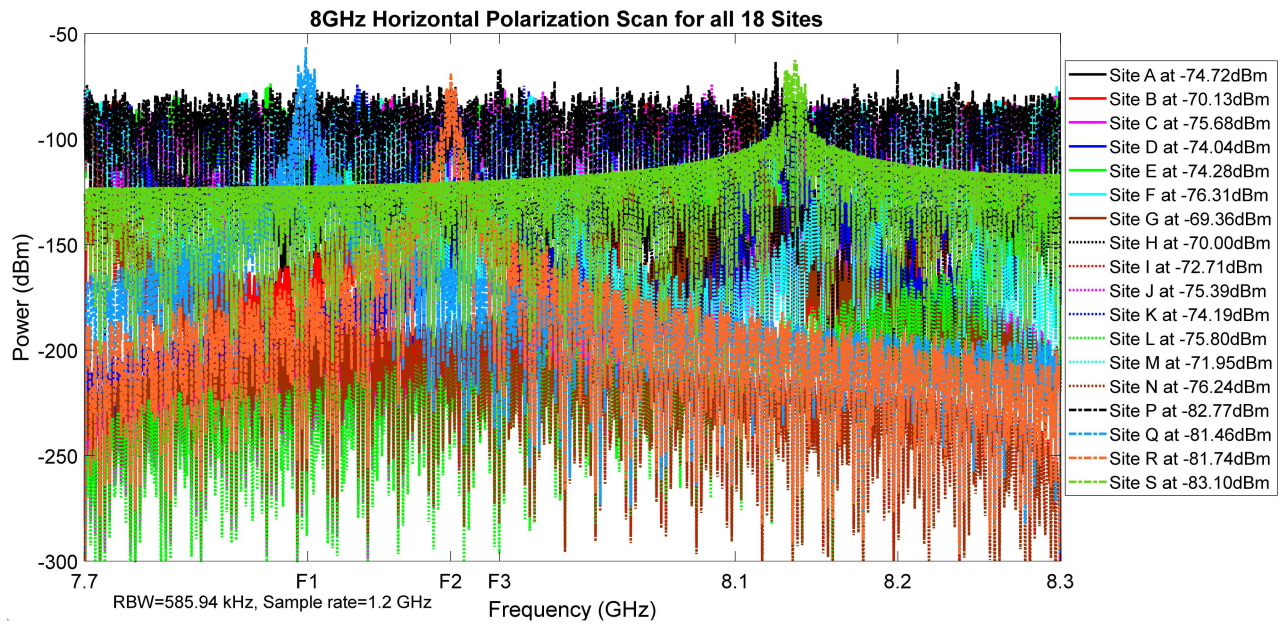


Figure 45. The 8 GHz horizontal polarization scan for all sites after denoising and applying the algorithm to all sites, including those without the potential to cause interference.

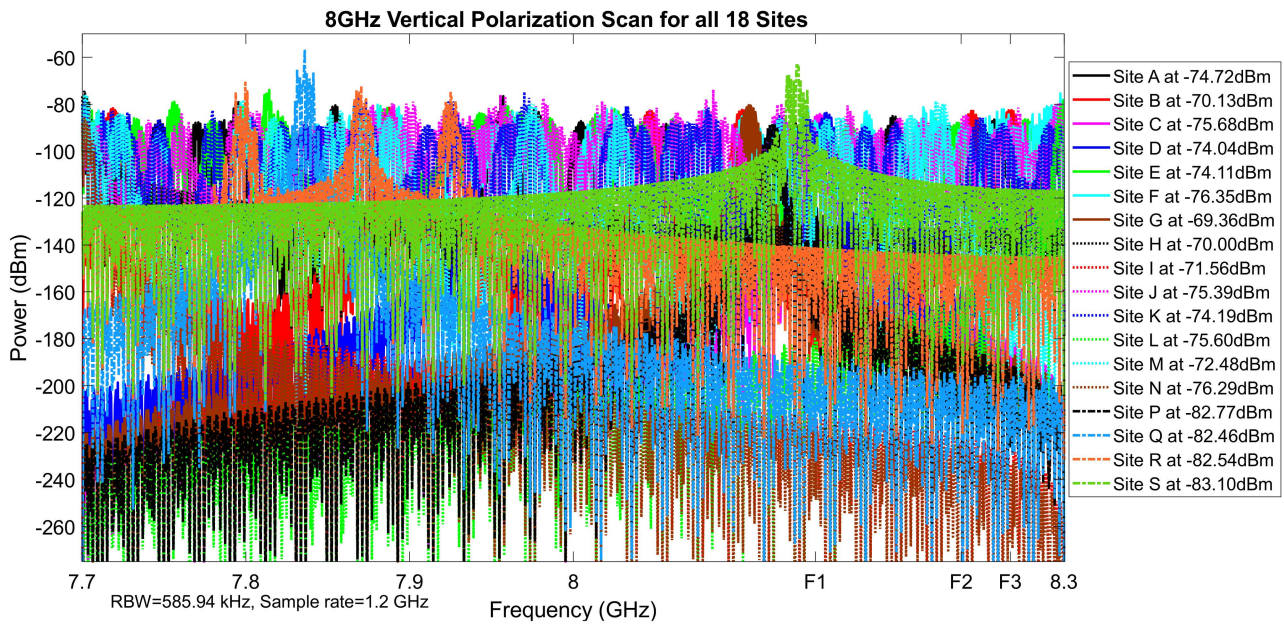


Figure 46. The 8 GHz vertical polarization scan for all sites after denoising and applying the algorithm to all sites, including those without the potential to cause interference.

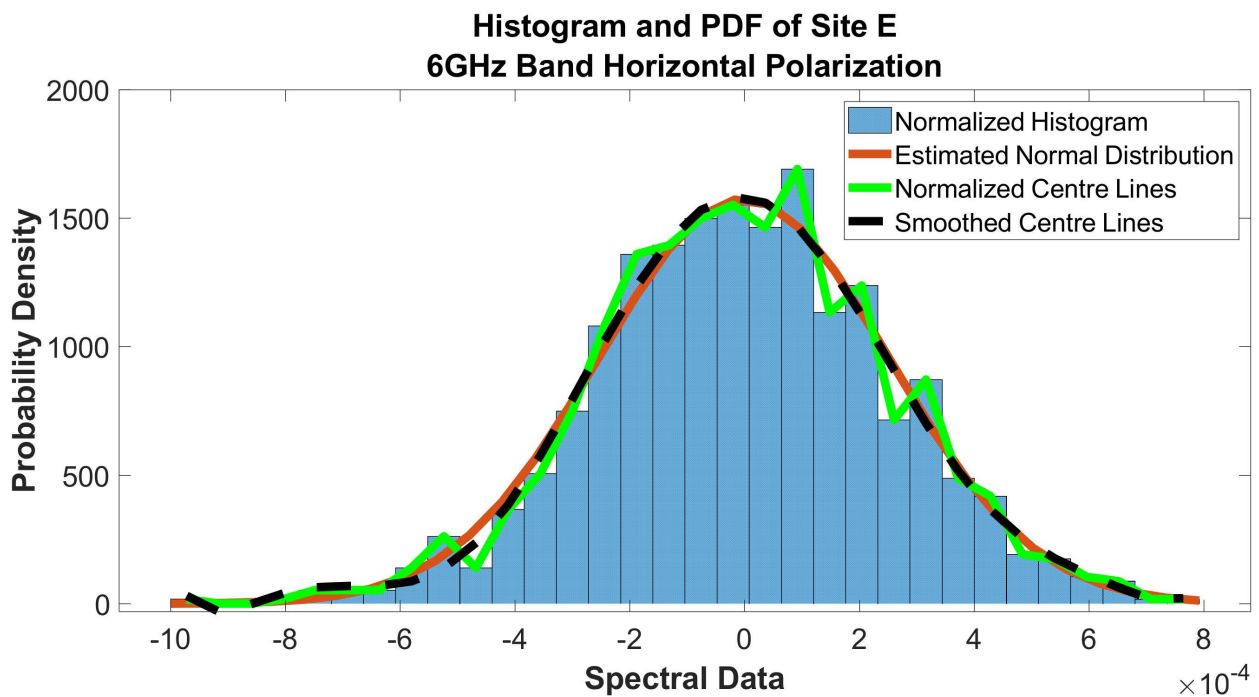


Figure 47. Histogram and PDF of site E at 6 GHz band horizontal polarization.

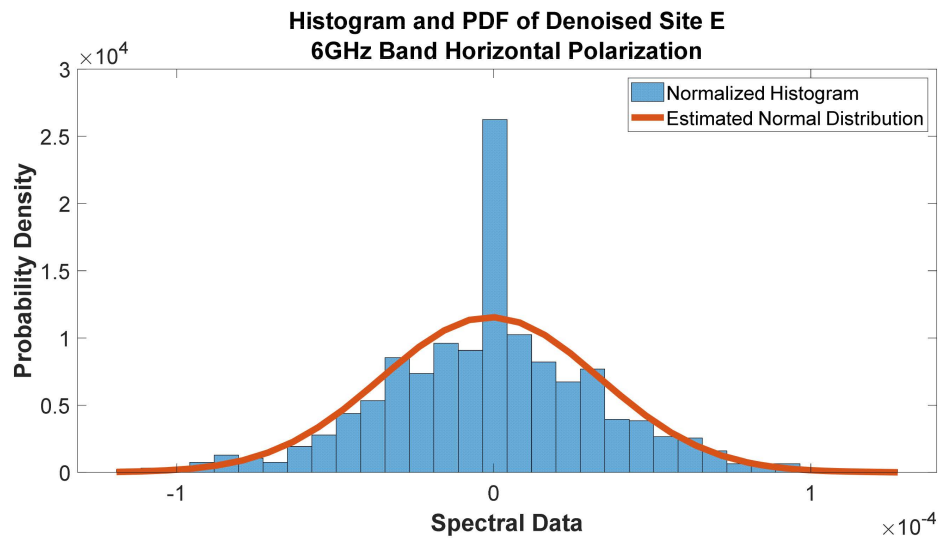


Figure 48. Histogram and PDF of Denoised Site E at 6 GHz band horizontal polarization.

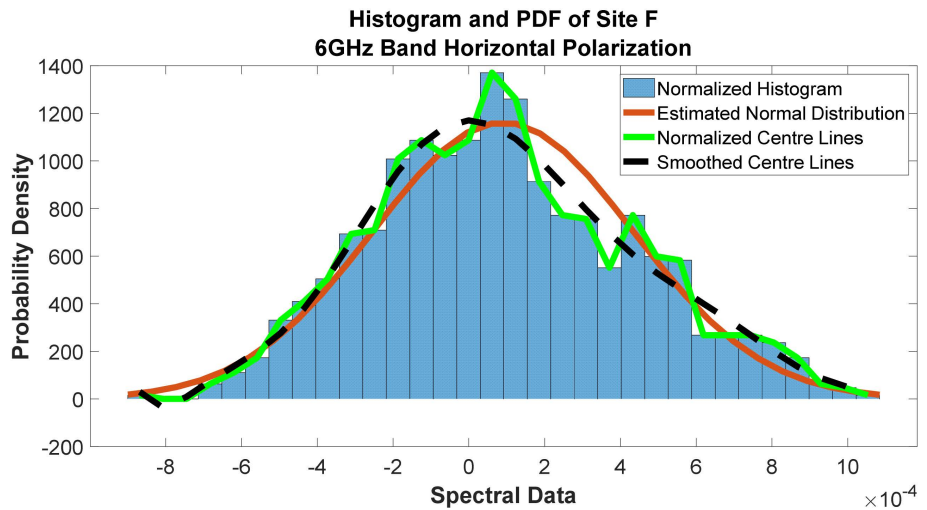


Figure 49. Histogram and PDF of site F at 6 GHz band horizontal polarization.

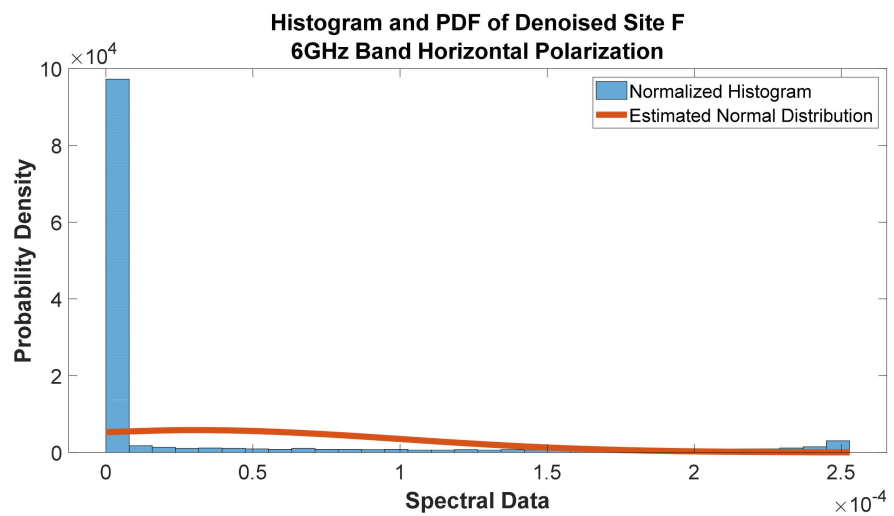


Figure 50. Histogram and PDF of Denoised Site F at 6 GHz band horizontal polarization.

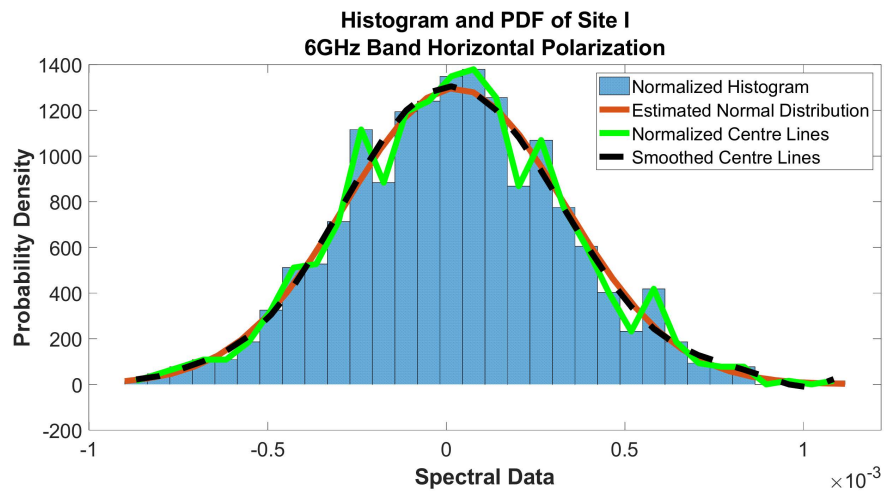


Figure 51. Histogram and PDF of site I at 6 GHz band horizontal polarization.

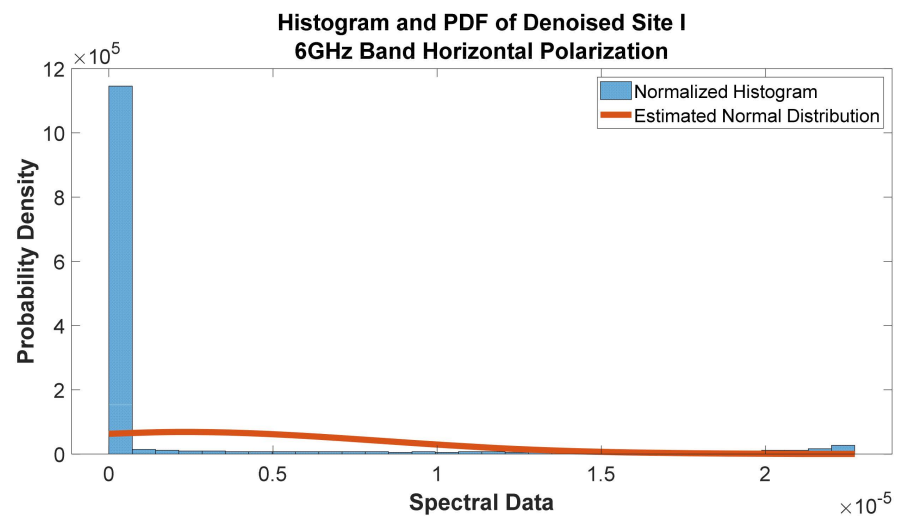


Figure 52. Histogram and PDF of Denoised Site I at 6 GHz band horizontal polarization.

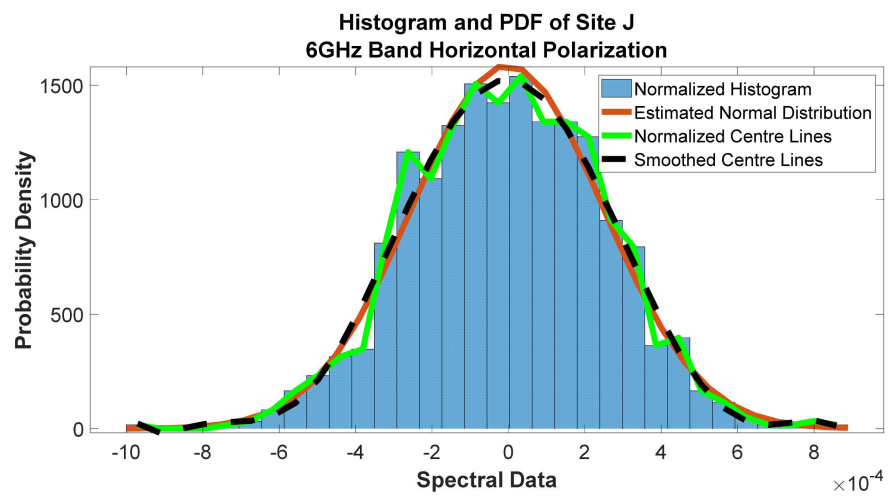


Figure 53. Histogram and PDF of site J at 6 GHz band horizontal polarization.

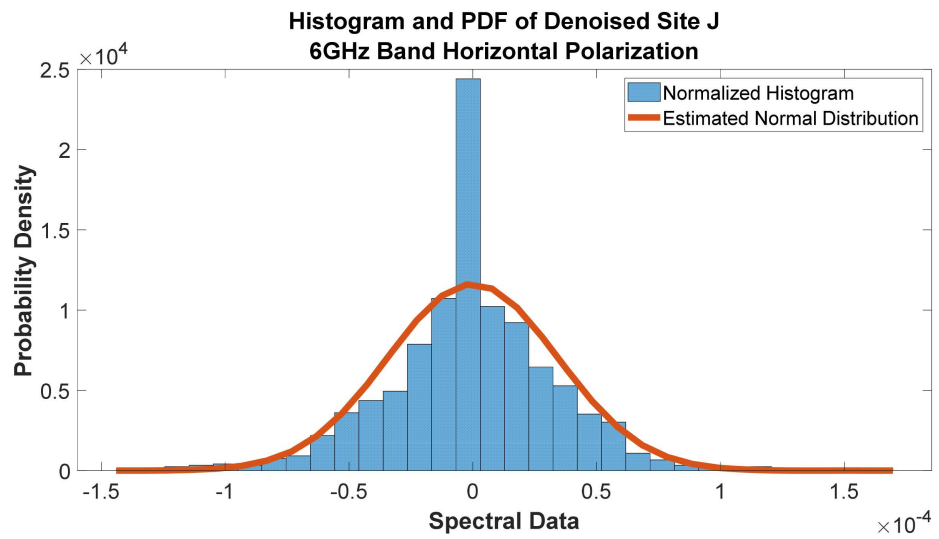


Figure 54. Histogram and PDF of Denoised Site J at 6 GHz band horizontal polarization.

Furthermore, Figure 52 presents the histogram and PDF of the denoised site I signal at the 6 GHz band horizontal polarization. The histogram and PDF of the site J signals at the 6 GHz band horizontal polarization are given in Figure 53. Additionally, the histogram and PDF of the denoised site J signals at the 6 GHz band horizontal polarization are presented in Figure 54. Finally, the statistical analysis showing the performances of the links before and after denoising at 6 GHz in horizontal polarization is summarized in Table 12.

Table 12. Statistical analysis showing the performances of the links before and after denoising at 6 GHz horizontal polarization.

Sites	Mean (10 ⁻⁶)		Standard Deviation (10 ⁻⁴)		Variance (10 ⁻⁸)		Interquartile Range (10 ⁻⁴)		Kurtosis		Skewness	
	before	after	before	after	before	after	before	after	before	after	before	after
A	0.0047	1.2407	2.5080	0.2955	6.2901	0.0873	3.4110	0.3292	3.0599	4.1251	-0.0179	-0.0720
B	-1.6533	-8.017 × 10 ⁻¹⁷	3.5103	0.2019	12.3220	0.0408	4.5058	0.1379	3.0296	4.8305	-0.0570	0.0031
C	-1.7686	-3.1209 × 10 ⁻¹⁷	2.3716	0.0779	5.6243	0.0061	3.2735	0	2.6843	13.8656	0.0315	0.0000
D	-4.6984	-3.9422 × 10 ⁻¹⁷	2.4144	0.1195	5.8295	0.0143	3.4200	0.0023	2.7889	8.7165	0.0224	0.0000
E	-1.7411	-1.0410	2.5321	0.3454	6.4113	0.1193	3.3590	0.4024	3.1917	3.7604	-0.0773	-0.0121
F	90.1250	30.9210	3.4356	0.6863	11.8030	0.4709	4.7799	0.0136	2.6339	6.3450	0.2292	2.1805
G	-0.2323	3.8942 × 10 ⁻¹⁷	3.4131	0.1399	11.6490	0.0196	4.8715	0.0024	2.8725	4.8953	0.0549	0.0004
H	24.6730	5.2349	3.5881	0.1517	12.8740	0.0230	4.9640	0.0417	2.9562	4.7004	0.0148	0.8181
I	24.3460	2.3590	3.0762	0.0584	9.4633	0.0034	4.1879	0	2.9850	7.5510	0.0751	2.4444
J	-2.2952	-3.8060 × 10 ⁻²	2.5141	0.3430	6.3205	0.1177	3.5579	0.3482	3.0303	5.2683	0.0058	0.1329
K	4.2881	4.3156 × 10 ⁻¹⁷	1.7027	0.0439	2.8993	0.0019	2.2939	0	3.1191	13.8656	0.0715	0.0000
L	-5.8571	-1.5371 × 10 ⁻¹⁷	2.4306	0.0983	5.9079	0.0097	3.2648	0	3.1706	7.9597	-0.1375	0.0000
M	6.3716	3.9639	3.0740	0.2415	9.4493	0.0583	4.2890	0.2106	2.7335	4.9027	-0.1359	-0.2865
N	6.3457	1.7088	2.1736	0.0423	4.7245	0.0018	2.9815	0	2.8333	7.5510	0.1472	2.4444
P	1.7134	0.6297	0.8349	0.0156	0.6970	0.0002	1.1084	0	3.1040	7.5510	0.1510	2.4444
Q	-3.0400	-3.3240 × 10 ⁻¹⁷	0.9557	0.0463	0.9133	0.0021	1.3107	0	2.9603	13.8656	0.0194	0.0000
R	-0.9157	2.5128 × 10 ⁻⁵	0.7289	0.0243	0.5313	0.0006	0.9962	0	2.9531	7.1513	0.0615	0.2360
S	-1.5575	-1.3105	0.4983	0.4571	0.2483	0.2089	0.6650	0.5393	3.0644	3.6404	0.0295	0.0159

4.7. Comparison of Results with Related Work

The results reported in Table 12 of this paper compare favorably with the results in Table 3 of Adeogun et al. [6]. The average interference probabilities for the 500 MHz sub-bands on the 8 GHz UWB spectrum modeled for interference sources with detected power ≥ -60 dBm are presented by Adeogun et al., where the denoised signal shows 0% for the 6.25 GHz, 6.75 GHz, 7.25 GHz, and 7.75 GHz, respectively. At 8.25 GHz and 8.75 GHz, the values of the standard deviations are 0.001% and 0.003%, respectively. Similarly, the mean values reported are 0%, 0.002%, 0%, 0.002%, 0.003%, and 0.004% for 6.25 GHz, 6.75 GHz, 7.25 GHz, 7.75 GHz, 8.25 GHz, and 8.75 GHz, respectively. Additionally, the waveforms of the denoised signal reported in Figures 41–46 of this paper compare fairly with the denoised processed results in Figures 3–8 of Section V in the work reported by Dias and Siqueira [62]. The observed variations are due mainly to the differences in the operating frequency bands and other dynamic environmental factors. Overall, the results reported in this paper pose huge application potentials in the design and development of standard RFI detection and mitigation techniques. Further discussion of the results is given in Section 4.8 of this paper.

4.8. Discussion of Results

The results of the extensive propagation measurements are briefly discussed as follows: The availability of the desired frequencies comprising the available (A) and not available (NA) frequencies captured by the spectrum analyzer was given in Table 5. Specifically, the availability of the desired frequencies for the 18 channels at 6 GHz: 5.945, 5.975, 6.005, 6.034, 6.093, 6.153 GHz, was observed. The available sites were A, C, E, I, L, N, and R, whereas the non-available sites were F, G, and H. The other sites that were tested have some available and non-available frequencies within the desired frequency spectrum. In Figures 5–10, the received power is fairly distributed across the sites. Site H has around 69 dBm in almost all scenarios, and site S has 86 dBm on average. The average power of channels P, Q, R, and S is distinct from the remaining 14 channels for all measurement scenarios. In particular, each average power of the four channels is more than -80 dBm. Interestingly, these four channels are located in Lagos State, a heavily dense urban environment. The remaining 14 channels are located in Kogi State, a moderately dense urban environment. The results indicate that channel F has both white and colored noise, and it is much noisier than the other channels. Therefore, no desired frequency may be used in channel F.

Additionally, the histogram and PDF of the frequency scan for sites A, B, C, and D, at 6, 7, and 8 GHz, are presented in Figures 11–34. Interestingly, the spectra data appear to follow a normal distribution for all scenarios. However, there are observed discrepancies with the distributions. These variations may be attributed to the varying degrees of interference from one site to another. Additionally, the cumulative distribution functions of the frequency scan for all sites at 6 GHz, 7 GHz, and 8 GHz are shown in Figures 26, 35 and 37–40. All cumulative distribution functions (CDFs) appear to follow the same trend for all measurement scenarios. The statistical error analyses of the frequency scan measurements for the 6 GHz, 7 GHz, and 8 GHz in horizontal and vertical polarization are presented in Tables 6–11. These include the mean absolute error (MAE), root mean squared error (RMSE), mean absolute percentage error (MAPE), relative absolute error (RAE), and the mean squared error (MSE). Error analysis for the estimated normal distribution (Y) and the estimated fitness curve (F) are tabulated. Here, the first five columns describe the error in PDF, and the last five columns describe the errors in the fitness curve for the 6 GHz, 7 GHz, and 8 GHz horizontal and vertical polarizations. Generally, the MAE and RMSE show the highest error values across tested criteria Y and F. On the other hand, the MAPE, RAE, and MSE show relatively lower values for both the Y and F scenarios. In all scenarios, site S appears to give the highest error statistics.

The results of the signal waveforms after noise removal are given in Figures 41–46. These comprise the frequency scan measurements for the sites after denoising and applying the algorithm to all sites, including those without the potential to cause interference.

Particularly, only Figures 41 and 42 are discussed for brevity. Figure 41 shows that the signal strength after denoising is about -67.5 dBm for the 6 GHz horizontal polarization scan in site G. This implies that the signals to be deployed must be at least -60 dBm, assuming less interference between signals that differ by 7.5 dBm. Additionally, the maximum signal strength is -80 dBm. This means that signals as low as -72.5 dBm can be deployed at the site without the fear of being interfered with by the existing signals. In the 6 GHz horizontal polarization, the possible sites of interference are G, H, J, K, P, Q, and S. The frequencies of interest labeled F1, F2, F3, F4, F5, and F6 are 5.945 GHz, 5.975 GHz, 6.005 GHz, 6.034 GHz, 6.093 GHz, and 6.153 GHz, respectively. The signal strength at all sites is reduced irrespective of the existing signals that may interfere with the yet-to-be-deployed signals. The maximum signal strength for the Gaussian noise was reduced from -69 dBm to -75 dBm after denoising.

In Figure 42, on-site G vertical polarization at 6 GHz, which has a -69.5 dBm noise level and existing signals of strength -67 dBm with possible interference with potential signals at F2, F3, F5, and F6, was reduced to -80 dBm at the F1 frequency and between 6.3 GHz and 6.4 GHz. This is lesser than the white noise before denoising and about the level of the white noise after denoising. The strength was lower than -80 dBm at other frequencies and as low as -200 dBm between the F5 and F6 frequencies. This was similar in all of the bands and polarizations. The sites with potential for interference had the existing signals aggregated and the overall signal strength minimized. The sites without existing signals were merely reproduced but with minimized signal strength.

Further to this, we compared the results for the frequency scan signals before and after denoising, as presented in Figures 47–54. These include the histogram and PDF of the actual signals collected at the sites. Here, the denoised signals are given in Figures 48, 50, 52 and 54. Specifically, Figures 48 and 54 tend to resemble a normal distribution curve far more than Figures 50 and 52, which do not follow a normal distribution curve at all. Compared to the signal waveforms before denoising, the waveforms obtained after denoising appear to not follow the normal distribution curve. In addition, the descriptive statistics of the frequency scan measurements are presented. The statistical analysis showing the performances of the links before and after denoising at 6 GHz, 7 GHz, and 8 GHz for the horizontal and vertical polarization is summarized in Table 12. These include the mean, standard deviation, variance, interquartile range, Kurtosis, and skewness.

The mean is the average of the data set. It can be seen from Table 12 that the mean values after denoising are lower than the mean values before denoising, except in site A. This shows that the noise level in each site was reduced when the algorithm was applied. The standard deviation measures how much a set of data is spread out around the mean/average. Additionally, it can be seen from Table 12 that the standard deviation values are lower after denoising. This is due to the aggregation of the existing signals by the algorithm, which tends to mix the existing signal with noise. Similarly, the variance measures the degree of variation around the mean/average. The interquartile range is a measure of where the bulk of the values lie. It can be seen that after denoising, the interquartile range values are lower than they were before denoising. This is also due to suppressing the noise level.

Skewness is a measure of a lack of symmetry in distribution. The level of skewness after denoising is greater than the level of skewness before denoising. Both of the values of before and after denoising have positive values. This indicates that there are heavy tails. However, kurtosis values after denoising are far greater than 3, indicating that the tails are heavier than the normal distribution. This means that the data after denoising does not follow the normal distribution. It can be seen from the estimated normal distribution curve and the actual histogram information that the data do not follow the normal distribution curve, as shown in Figures 48, 50, 52 and 54. This implies that the error between the estimated curve and the actual data after denoising will be higher than before denoising. Therefore, the site data after denoising cannot be accurately estimated with a normal distribution curve. Additionally, it can be seen from the probability density axis of the

graph that the values are far greater after denoising than before denoising. This is due to the aggregating of signals and noise in the sites. Finally, the spectral data axis shows that the values are lower after denoising. This is due to the suppression of the prior existing signal strengths that may pose as interference for the desired signals to be deployed.

5. Conclusions

This paper reports the performance evaluation of radio frequency interference measurements conducted at 6 GHz, 7 GHz, and 8 GHz. Extensive field measurements were conducted to experimentally detect and evaluate radio frequency interference in microwave links using a spectrum analyzer. The actual frequency scan measurements for the horizontal and vertical polarization and the analyzed frequency scans for the tested sites were presented. The probability density functions of the frequency scans covering the normalized histogram estimated normal distribution, normalized center lines, and the smoothed center lines were shown. Additionally, the cumulative distribution functions of the frequency scans for the tested sites for both polarizations were reported. The statistical error characteristics of the frequency scan comprising the mean absolute error (MAE), root mean squared error (RMSE), mean absolute percentage error (MAPE), relative absolute error (RAE), mean squared error (MSE), each for the estimated normal distribution and the estimated fitness curve was derived. Further to this, the performance of the links was accessed using several error metrics, and the results revealed the presence of interference on the tested links. Additionally, the analysis of the frequency scan signals before and after the noise removal was demonstrated. The denoised signals compare favorably to related results in the existing literature. Last, the frequency scans would be beneficial in evaluating RFI measurements and spectrum planning in a related wireless environment. Future work would examine similar measurements in ISM bands and wideband scan RFI from 1 GHz to over 10 GHz. Additionally, the measured data could be used in developing robust RFI detection, mitigation, and optimization techniques.

Author Contributions: The manuscript was written through the contributions of all authors. G.U.U., A.L.I. and M.A.A. were responsible for the conceptualization of the topic; article gathering and sorting were conducted by G.U.U., A.L.I. and M.A.A.; manuscript writing and original drafting and formal analysis were carried out by A.L.I.; writing of the review and editing was completed by A.L.I.; M.A.A. and A.L.I. led the overall research activity. All authors have read and agreed to the published version of the manuscript.

Funding: This research received no external funding.

Institutional Review Board Statement: Not applicable.

Informed Consent Statement: Not applicable.

Data Availability Statement: The data that support the findings of this study are available from the corresponding author upon reasonable request.

Acknowledgments: The work of Agbotiname Lucky Imoize is supported by the Nigerian Petroleum Technology Development Fund (PTDF) and the German Academic Exchange Service (DAAD) through the Nigerian-German Postgraduate Program under Grant 57473408.

Conflicts of Interest: The authors declare that they have no conflicts of interest.

Abbreviations

APU	Analog processing units
BS	Base stations
CDF	Cumulative distribution function
CDIP	Chromatic dispersion-induced power fading
CSA	Cyclic spectrum analysis
CSS	Compressive statistical sensing

DPU	Digital processing unit
DSB	Double-sideband
EDFA	Erbium-doped fiber amplifier
FA	Factor analysis
FFT	Fast Fourier transform
IFFT	Inverse fast Fourier transform
ISTFT	Inverse short-time Fourier transform
ITU	International Telecommunication Union
LLMMSE	Locally adaptive linear minimum mean square error
MAE	Mean absolute error
MAPE	Mean absolute percentage error
MSE	Mean squared error
NQR	Nuclear quadrupole resonance
OLA	Overlap-Add
PAP	Path angular profile
PAS	Power angular spectrum
PCB	Printed circuit board
PDF	Probability density function
RAE	Relative absolute error
RFI	Radio frequency interference
RMSE	Root mean squared error
SMAP	Soil moisture active and passive
SFD	Spectral flux density
SMF	Single-mode fiber
STFT	Short-time Fourier transformations
WAIM	Wide-angle impedance matching
WOLA	Weighted Overlap-Add

References

- Djuric, N.; Antic, D.; Kljajic, D.; Fanti, A.; Djuric, S. The SEMONT's database support for quad-band monitoring of EMF exposure. *Measurement* **2017**, *99*, 78–89. [[CrossRef](#)]
- Zheng, G.; Krikidis, I.; Masouros, C.; Timotheou, S.; Toumpakaris, D.-A.; Ding, Z. Rethinking the role of interference in wireless networks. *IEEE Commun. Mag.* **2014**, *52*, 152–158. [[CrossRef](#)]
- Ughegbe, G.U.; Adelabu, M.A.; Imoize, A.L. Experimental data on radio frequency interference in microwave links using frequency scan measurements at 6 GHz, 7 GHz, and 8 GHz. *Data Brief* **2021**, *35*, 106916. [[CrossRef](#)] [[PubMed](#)]
- Tarongí, J.M.; Camps, A. Radio frequency interference detection and mitigation algorithms based on spectrogram analysis. *Algorithms* **2011**, *4*, 239–261. [[CrossRef](#)]
- Cucho-Padin, G.; Wang, Y.; Li, E.; Waldrop, L.; Tian, Z.; Kamalabadi, F.; Perillat, P. Radio frequency interference detection and mitigation using compressive statistical sensing. *Radio Sci.* **2019**, *54*, 986–1001. [[CrossRef](#)]
- Adeogun, R.; Berardinelli, G.; Rodriguez, I.; Mogensen, P.E.; Razzaghpour, M. Measurement and analysis of radio frequency interference in the UWB spectrum. In Proceedings of the 90th Vehicular Technology Conference, Honolulu, HI, USA, 22–25 September 2019; pp. 19–23. [[CrossRef](#)]
- Babich, F.; Buttazzoni, G.; Vatta, F.; Comisso, M. Energy-constrained design of joint NOMA-diversity schemes with imperfect interference cancellation. *Sensors* **2021**, *21*, 4194. [[CrossRef](#)]
- Henry, V. ATS-6 Radio frequency interference measurement experiment. *IEEE Trans. Aerosp. Electron. Syst.* **1975**, *AES-11*, 1059–1066. [[CrossRef](#)]
- Fletcher, J.C.; Johannsen, K.G.; Henry, V.F. Systems and Methods for Determining Radio Frequency Interference. U.S. Patent 4,119,964, 10 October 1978.
- Wu, Q.; Zhang, R. Intelligent reflecting surface enhanced wireless network: Joint active and passive beamforming design. In Proceedings of the IEEE Global Communications Conference (GLOBECOM), Abu Dhabi, United Arab Emirates, 9–13 December 2018; pp. 1–6.
- Huang, C.; Zappone, A.; Alexandropoulos, G.C.; Debbah, M.; Yuen, C. Reconfigurable intelligent surfaces for energy efficiency in wireless communication. *IEEE Trans. Wirel. Commun.* **2019**, *18*, 4157–4170. [[CrossRef](#)]
- Zhao, J. A survey of intelligent reflecting surfaces (IRSs): Towards 6G wireless communication networks. *arXiv* **2019**, arXiv:1907.04789.
- Wang, J.; Tang, W.; Han, Y.; Jin, S.; Li, X.; Wen, C.-K.; Cheng, Q.; Cui, T.J. Interplay between RIS and AI in wireless communications: Fundamentals, architectures, applications, and open research problems. *arXiv* **2021**, arXiv:2021.3087259.
- Zhou, S.; Xu, W.; Wang, K.; Di Renzo, M.; Alouini, M.-S. Spectral and energy efficiency of IRS-assisted MISO communication with hardware impairments. *IEEE Wirel. Commun. Lett.* **2020**, *9*, 1366–1369. [[CrossRef](#)]

15. Querol, J.; Perez, A.; Camps, A. A review of RFI mitigation techniques in microwave radiometry. *Remote. Sens.* **2019**, *11*, 3042. [[CrossRef](#)]
16. Virk, U.T.; Nguyen, S.L.H.; Haneda, K. Multi-frequency power angular spectrum comparison for an indoor environment. In Proceedings of the 11th European Conference on Antennas and Propagation, Paris, France, 19–24 March 2017; pp. 3389–3393.
17. Rajabi, H.; Aksoy, M. Characteristics of the L-band radio frequency interference environment based on SMAP radiometer observations. *IEEE Geosci. Remote. Sens. Lett.* **2019**, *16*, 1736–1740. [[CrossRef](#)]
18. Ionescu, M.; Lavery, D.; Edwards, A.; Sillekens, E.; Galdino, L.; Semrau, D.; Killely, R.; Pelouch, W.; Barnes, S.; Bayvel, P. 74.38 Tb/s transmission over 6300 km single mode fiber with hybrid EDFA/Raman amplifiers. In Proceedings of the Optical Fiber Communications Conference and Exhibition, San Diego, CA, USA, 3–7 March 2019. [[CrossRef](#)]
19. Jaroenjittichai, P.; Punyawarin, S.; Singwong, D.; Somboonpon, P.; Prasert, N.; Bandudej, K.; Kempet, P.; Leckngam, A.; Poshyachinda, S.; Soonthornthum, B.; et al. Radio frequency interference site survey for thai radio telescopes. *J. Phys. Conf. Ser.* **2017**, *901*, 12062. [[CrossRef](#)]
20. Zhu, S.; Fan, X.; Li, M.; Zhu, N.H.; Li, W. Dual-chirp microwave waveform transmitter with elimination of power fading for one-to-multibase station fiber transmission. *Opt. Lett.* **2020**, *45*, 1285–1288. [[CrossRef](#)]
21. Zu, H.-R.; Wu, B.; Zhao, Y.-T.; Cheng, Q.S.; Lu, W.-B. Dual-frequency-scanning broadband antenna based on Z-shape spoof surface plasmon polaritons. *Appl. Phys. Express* **2019**, *12*, 084001. [[CrossRef](#)]
22. Huang, Q.; Enomoto, T.; Seto, S.; Araki, K.; Fan, J.; Hwang, C. A Transfer function based calculation method for radio frequency interference. *IEEE Trans. Electromagn. Compat.* **2019**, *61*, 1280–1288. [[CrossRef](#)]
23. Ibrahim, M.; Parrish, D.J.; Brown, T.W.C.; McDonald, P.J. Decision tree pattern recognition model for radio frequency interference suppression in NQR experiments. *Sensors* **2019**, *19*, 3153. [[CrossRef](#)]
24. Han, H.; Zhao, J.; Niyato, D.; Di Renzo, M.; Pham, Q.-V. Intelligent reflecting surface aided network: Power control for physical-layer broadcasting. In Proceedings of the International Conference on Communications, Dublin, Ireland, 7–11 June 2020; pp. 1–7.
25. Wu, Q.; Zhang, R. Intelligent reflecting surface enhanced wireless network via joint active and passive beamforming. *IEEE Trans. Wirel. Commun.* **2019**, *18*, 5394–5409. [[CrossRef](#)]
26. Gui, G.; Liu, M.; Tang, F.; Kato, N.; Adachi, F. 6G: Opening new horizons for integration of comfort, security, and intelligence. *IEEE Wirel. Commun.* **2020**, *27*, 126–132. [[CrossRef](#)]
27. El Mossallamy, M.A.; Zhang, H.; Song, L.; Seddik, K.G.; Han, Z.; Li, G.Y. Reconfigurable intelligent surfaces for wireless communications: Principles, challenges, and opportunities. *IEEE Trans. Cogn. Commun. Netw.* **2020**, *6*, 990–1002. [[CrossRef](#)]
28. Wu, Q.; Zhang, R. Towards smart and reconfigurable environment: Intelligent reflecting surface aided wireless network. *IEEE Commun. Mag.* **2020**, *58*, 106–112. [[CrossRef](#)]
29. Jung, M.; Saad, W.; Jang, Y.; Kong, G.; Choi, S. Performance analysis of large intelligent surfaces (LISs): Asymptotic data rate and channel hardening effects. *IEEE Trans. Wirel. Commun.* **2020**, *19*, 2052–2065. [[CrossRef](#)]
30. Yan, W.; Yuan, X.; Kuai, X. Passive beamforming and information transfer via large intelligent surface. *IEEE Wirel. Commun. Lett.* **2019**, *9*, 533–537. [[CrossRef](#)]
31. Wu, Q.; Zhang, R. Weighted sum power maximization for intelligent reflecting surface aided SWIPT. *IEEE Wirel. Commun. Lett.* **2020**, *9*, 586–590. [[CrossRef](#)]
32. Basar, E.; Di Renzo, M.; De Rosny, J.; Debbah, M.; Alouini, M.-S.; Zhang, R. Wireless communications through reconfigurable intelligent surfaces. *IEEE Access* **2019**, *7*, 116753–116773. [[CrossRef](#)]
33. Liaskos, C.; Nie, S.; Tsioliaridou, A.; Pitsillides, A.; Ioannidis, S.; Akyildiz, I. A new wireless communication paradigm through software-controlled metasurfaces. *IEEE Commun. Mag.* **2018**, *56*, 162–169. [[CrossRef](#)]
34. Hum, S.V.; Perruisseau-Carrier, J. Reconfigurable reflectarrays and array lenses for dynamic antenna beam control: A review. *IEEE Trans. Antennas Propag.* **2014**, *62*, 183–198. [[CrossRef](#)]
35. Tan, X.; Sun, Z.; Koutsonikolas, D.; Jornet, J.M. Enabling indoor mobile millimeter-wave networks based on smart reflect-arrays. In Proceedings of the Conference on Computer Communications, Honolulu, HI, USA, 15–19 April 2018; pp. 270–278.
36. Foo, S. Liquid Crystal Reconfigurable Metasurface Reflector Antenna. In Proceedings of the International Symposium on Antennas and Propagation & USNC/URSI National Radio Science Meeting, San Diego, CA, USA, 9–14 July 2017.
37. Shen, H.; Xu, W.; Gong, S.; He, Z.; Zhao, C. Secrecy Rate Maximization for Intelligent Reflecting Surface Assisted Multi-Antenna Communications. *IEEE Commun. Lett.* **2019**, *23*, 1488–1492. [[CrossRef](#)]
38. Zhang, Z.; Zhang, C.; Jiang, C.; Jia, F.; Ge, J.; Gong, F. Improving physical layer security for reconfigurable intel-ligent surface aided NOMA 6G networks. *arXiv* **2021**, arXiv:2101.06948.
39. Imoize, A.; Adediji, O.; Tandiya, N.; Shetty, S. 6G enabled smart infrastructure for sustainable society: Opportunities, challenges, and research roadmap. *Sensors* **2021**, *21*, 1709. [[CrossRef](#)] [[PubMed](#)]
40. Hong, S.; Pan, C.; Ren, H.; Wang, K.; Nallanathan, A. Artificial-noise-aided secure MIMO wireless communications via intelligent reflecting surface. *IEEE Trans. Commun.* **2020**, *68*, 7851–7866. [[CrossRef](#)]
41. Matthaiou, M.; Yurduseven, O.; Ngo, H.Q.; Morales-Jimenez, D.; Cotton, S.L.; Fusco, V.F. The road to 6G: Ten physical layer challenges for communications engineers. *IEEE Commun. Mag.* **2021**, *59*, 64–69. [[CrossRef](#)]
42. Yang, H.; Cao, X.; Yang, F.; Gao, J.; Xu, S.; Li, M.; Chen, X.; Zhao, Y.; Zheng, Y.; Li, S. A programmable metasurface with dynamic polarization, scattering and focusing control. *Sci. Rep.* **2016**, *6*, 35692. [[CrossRef](#)]

43. Nadeem, Q.-U.-A.; Kammoun, A.; Chaaban, A.; Debbah, M.; Alouini, M.-S. Intelligent reflecting surface assisted wireless communication: Modeling and channel estimation. *arXiv* **2019**, arXiv:1906.02360.
44. Wang, Z.; Liu, L.; Cui, S. Channel estimation for intelligent reflecting surface assisted multiuser communications. In Proceedings of the Wireless Communications and Networking Conference, Seoul, Korea, 25–28 May 2020. [[CrossRef](#)]
45. Oh, S.-H.; Myung, N.-H. MIMO channel estimation method using ray-tracing propagation model. *Electron. Lett.* **2005**, *41*, 40–41. [[CrossRef](#)]
46. Taha, A.; Alrabeiah, M.; Alkhateeb, A. Enabling large intelligent surfaces with compressive sensing and deep learning. *IEEE Access* **2021**, *9*, 44304–44321. [[CrossRef](#)]
47. Qin, Z.; Ye, H.; Li, G.Y.; Juang, B.-H.F. Deep learning in physical layer communications. *IEEE Wirel. Commun.* **2019**, *26*, 93–99. [[CrossRef](#)]
48. Yang, Z.; Chen, M.; Wong, K.-K.; Poor, H.V.; Cui, S. Federated learning for 6G: Applications, challenges, and opportunities. *arXiv* **2021**, arXiv:2101.01338.
49. Ibhaze, A.E.; Imoize, A.L.; Ajose, S.O.; John, S.N.; Ndujiuba, C.U.; Idachaba, F.E. An empirical propagation model for path loss prediction at 2100MHz in a dense urban environment. *Indian J. Sci. Technol.* **2017**, *10*, 1–9. [[CrossRef](#)]
50. Imoize, A.L.; Orolu, K.; Atayero, A.A.-A. Analysis of key performance indicators of a 4G LTE network based on experimental data obtained from a densely populated smart city. *Data Brief* **2020**, *29*, 105304. [[CrossRef](#)]
51. Fanti, A.; Schirru, L.; Casu, S.; Lodi, M.B.; Riccio, G.; Mazzarella, G. Improvement and Testing of Models for Field Level Evaluation in Urban Environment. *IEEE Trans. Antennas Propag.* **2020**, *68*, 4038–4047. [[CrossRef](#)]
52. Anritsu. *RF Interference Hunting Techniques—Spot, Find, Fix*; Anritsu Co.: Atsugi-shi, Japan, 2014; pp. 1–20.
53. Bird, J. *Engineering Mathematics*, 5th ed.; Newness: Los Angeles, CA, USA, 2010.
54. Moorer, J.A. A note on the implementation of audio processing by short-term fourier transform. In Proceedings of the Workshop on Applications of Signal Processing to Audio and Acoustics (WASPAA), New Paltz, NY, USA, 15–18 October 2017; Volume 127, pp. 156–159.
55. Zhivomirov, H. On the development of STFT-analysis and ISTFT-synthesis routines and their practical implementation. *TEM J.* **2019**, *8*, 56–64. [[CrossRef](#)]
56. Frigo, M.; Johnson, S. The design and implementation of FFTW3. *Proc. IEEE* **2005**, *93*, 216–231. [[CrossRef](#)]
57. Johnson, S.; Frigo, M. A modified split-radix FFT with fewer arithmetic operations. *IEEE Trans. Signal Process.* **2007**, *55*, 111–119. [[CrossRef](#)]
58. Johnson, S.G.; Frigo, M. Implementing FFTs in Practice. 2008. Available online: <http://cnx.org/content/m16336/> (accessed on 19 July 2021).
59. Ouelha, S.; Touati, S.; Boashash, B. An efficient inverse short-time Fourier transform algorithm for improved signal reconstruction by time-frequency synthesis: Optimality and computational issues. *Digit. Signal Process.* **2017**, *65*, 81–93. [[CrossRef](#)]
60. Ponomareva, O.; Ponomarev, A.; Ponomarev, V. Evolution of Forward and Inverse Discrete Fourier Transform. In Proceedings of the East-West Design & Test Symposium (EWDTS), Kazan, Russia, 14–17 September 2018; pp. 1–5.
61. Prabhu, K.M.M. *Window Functions and Their Applications in Signal Processing*; Taylor & Francis: Boca Raton, FL, USA, 2014.
62. Dias, M.H.C.; Siqueira, G.L. Improving 900 MHz outdoor measured wideband power delay profiles with wavelet denoising. In Proceedings of the SMBO/IEEE MTT-S International Microwave and Optoelectronics Conference, Salvador, Brazil, 29 October–1 November 2007; pp. 157–161.